nature genetics

ARTICLES

https://doi.org/10.1038/s41588-021-00830-1

Functional and structural basis of extreme conservation in vertebrate 5′ untranslated regions

Gun Woo Byeon[1,2], Elif Sarinay Cenik[1,2,4], Lihua Jiang[1], Hua Tang[1], Rhiju Das[3] and Maria Barna[1,2]✉

The lack of knowledge about extreme conservation in genomes remains a major gap in our understanding of the evolution of gene regulation. Here, we reveal an unexpected role of extremely conserved 5′ untranslated regions (UTRs) in noncanonical translational regulation that is linked to the emergence of essential developmental features in vertebrate species. Endogenous deletion of conserved elements within these 5′ UTRs decreased gene expression, and extremely conserved 5′ UTRs possess *cis*-regulatory elements that promote cell-type-specific regulation of translation. We further developed in-cell mutate-and-map (icM²), a new methodology that maps RNA structure inside cells. Using icM², we determined that an extremely conserved 5′ UTR encodes multiple alternative structures and that each single nucleotide within the conserved element maintains the balance of alternative structures important to control the dynamic range of protein expression. These results explain how extreme sequence conservation can lead to RNA-level biological functions encoded in the untranslated regions of vertebrate genomes.

One of the most fascinating findings from the comparative analysis of vertebrate genomes is the existence of extreme sequence conservation in noncoding regions, at levels often greater than in coding regions with perfectly invariant polypeptides[1–11]. These regions are undergoing strong purifying selection in humans and are not merely mutational cold spots[12]. However, the fundamental problem that was initially raised a decade ago still remains unsolved: why does such extreme conservation arise during evolution, and what are the functional roles for such sequences in the genome?

To date, efforts to understand the phenomenon of extreme conservation have focused heavily on intergenic sequences, suggesting possible roles for these elements as transcriptional enhancers[13–15]. However, early in vivo knockout studies paradoxically yielded viable mice lacking grossly deleterious phenotypes, raising uncertainties about the relevance and contribution of highly conserved elements to organismal development[16,17]. It is only more recently that mice with loss of single or pairwise deletions of ultraconserved enhancer elements have been shown to produce more subtle developmental phenotypes due to the impact on the transcription of neighboring genes[18,19].

However, beyond its importance in transcriptional regulation, the biological meaning of extreme conservation in post-transcriptional regulation remains largely unknown. While a few examples, such as the functional roles for ultraconserved regions transcribed as long noncoding RNAs or alternatively spliced poison cassette exons, have been described[20–24], RNA-level mechanisms for extreme conservation have not been widely explored. The observation of extreme sequence conservation across extended stretches of 5′ UTRs suggests the presence of specialized translational *cis*-regulatory elements. In a paradigmatic example, the *Hoxa9* 5′ UTR contains an ~650-nucleotide extremely conserved region that mediates noncanonical translation initiation through a structured internal ribosome entry site (IRES)-like RNA element[25]. Knockout of an ~150-base pair (bp) functional element within this conserved region in mice results in diminished spatiotemporal Hoxa9 protein expression and a pronounced axial skeleton phenotype leading to a homeotic transformation, demonstrating how 5′ UTR RNA sequences important for specialized translational regulation in the developing embryo can undergo extraordinary negative selection. We were thus inspired to ask if there could be a broader, systematic trend for extreme conservation, to reveal currently unknown translational regulatory sequences, and, conversely, if such regulatory sequences could help to explain the functional basis of extreme noncoding conservation in messenger RNAs.

Results

Hyperconserved 5′ UTRs in vertebrate genomes. To address the function of extreme noncoding conservation for mRNA 5′ UTRs, we used the conservation pattern of the aforementioned *Hoxa9* 5′ UTR as our archetype in selecting a set of other 5′ UTRs in the genome. The length of the extremely conserved stretch in *Hoxa9* 5′ UTR is ~650 nucleotides; the size of the functional element within the conserved stretch is around 350 nucelotides[25]. We used PhastCons with a log of the odds score (LOD) minimum of 500, which marked large blocks of extremely conserved sequences throughout the genome that are 100 nucleotides long, on average[26]. Using mouse RefSeq gene annotations, we intersected mouse 5′ UTRs with the LOD ≥ 500 PhastCons elements (representing the top 8.25% of all PhastCons elements identified in the genome), requiring at least ≥250 nucleotides overlap. This resulted in a set of 589 5′ UTRs for 499 genes (Fig. 1a and Supplementary Table 1). The median nucleotide identity between mouse and human genomes in the conserved regions in the selected 5′ UTRs is 92.3% (80% identity at 5th percentile). The average total length and the average number of nucleotides overlapping PhastCons elements for these 589 5′ UTRs are 674 and 389 nucleotides, respectively, and they tend to be found more frequently closer to the start codon than to the 5′ end (Extended Data Fig. 1a–c). For the remainder of the text, we will refer to these 589 5′ UTRs as hyperconserved 5′ UTRs (h5UTRs) and the LOD ≥ 500

[1]Department of Genetics, Stanford University School of Medicine, Stanford, CA, USA. [2]Department of Developmental Biology, Stanford University School of Medicine, Stanford, CA, USA. [3]Department of Biochemistry, Stanford University School of Medicine, Stanford, CA, USA. [4]Present address: Department of Molecular Biosciences, University of Texas Austin, Austin, TX, USA. ✉e-mail: mbarna@stanford.edu

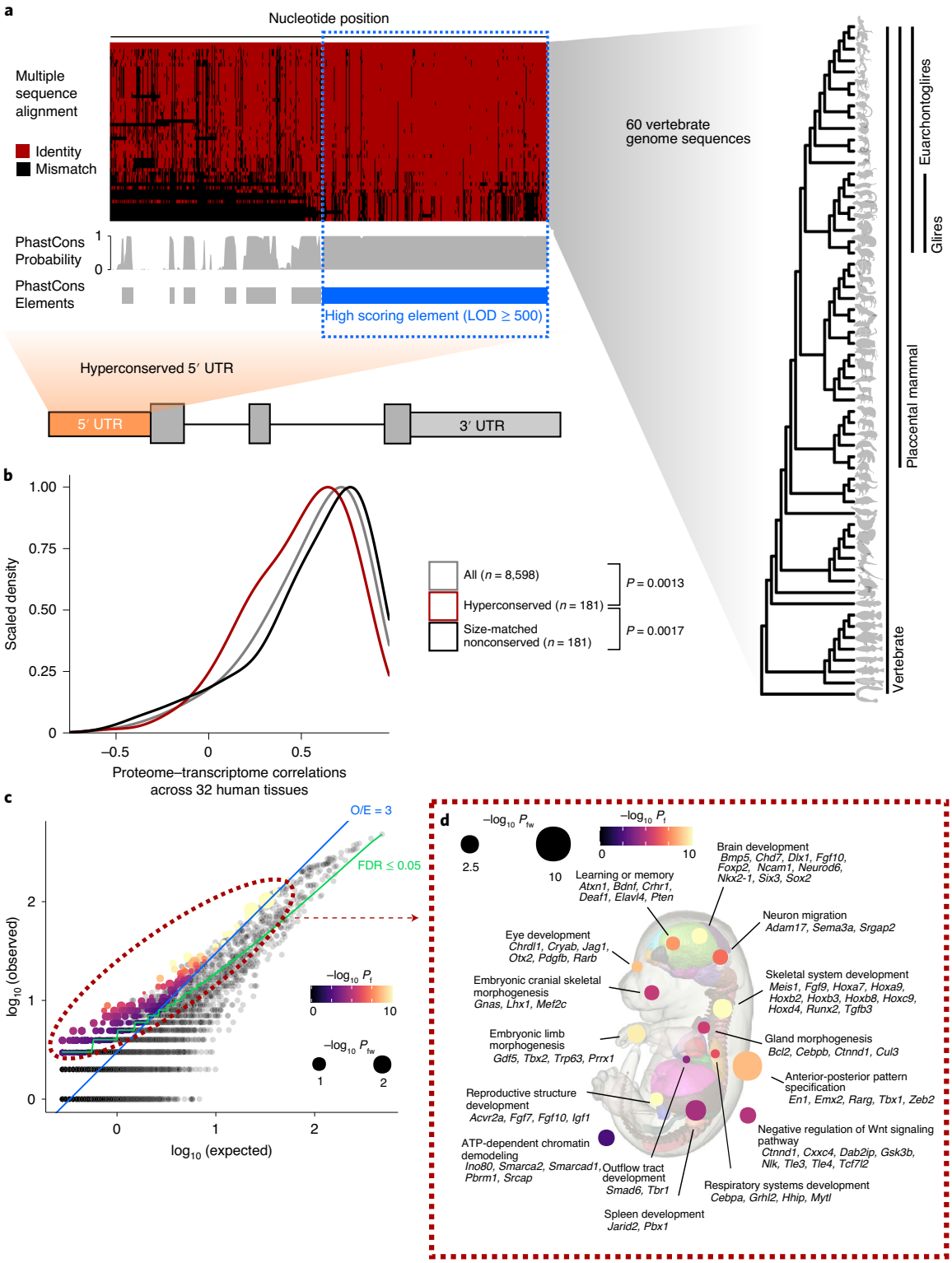

Fig. 1 | Hyperconserved 5′ UTRs in vertebrate genomes. a, Schematic illustrating selection of hyperconserved vertebrate 5′ UTRs. We begin with 60-way multiple species alignment of vertebrate genomes, its per-nucleotide PhastCons probabilities and conserved element prediction tracks. High-scoring (LOD ≥ 500) PhastCons elements are overlapped with RefSeq annotated mouse 5′ UTRs. We define those with overlap ≥250 nucleotides to be hyperconserved (also see Supplementary Table 1). **b**, Distributions of cross-tissue transcriptome–proteome correlations (GTEx Consortium data across 32 human tissues) for all genes, genes with h5UTRs or genes with size-matched nonconserved 5′ UTRs. Indicated *P* values are from two-sided Wilcoxon rank-sum tests for cross-tissue correlation values between h5UTR genes and all genes, or between h5UTR genes and size-matched nonconserved controls. **c**, Scatter plot illustrating the term enrichment strategy and criteria. The *x* axis and *y* axis plot the expected (E) and the observed (O) number of genes for each term. Blue dashed line indicates the minimum observed/expected (O/E) ratio cut-off of 3. Green line indicates expected and observed counts where two-tailed Fisher's test *P* value (P_f) is estimated to have FDR = 0.05. Neighbor-weighted test *P* value (P_{fw}) ≤0.05 is further used as an additional cut-off. The final set of enriched terms passing the filter is colored by P_f and sized by P_{fw}. **d**, Visualization of representative gene ontology terms significantly enriched for the h5UTRs according to criteria in **c**. A number of genes mapping to each term are also displayed (also see Supplementary Table 2).

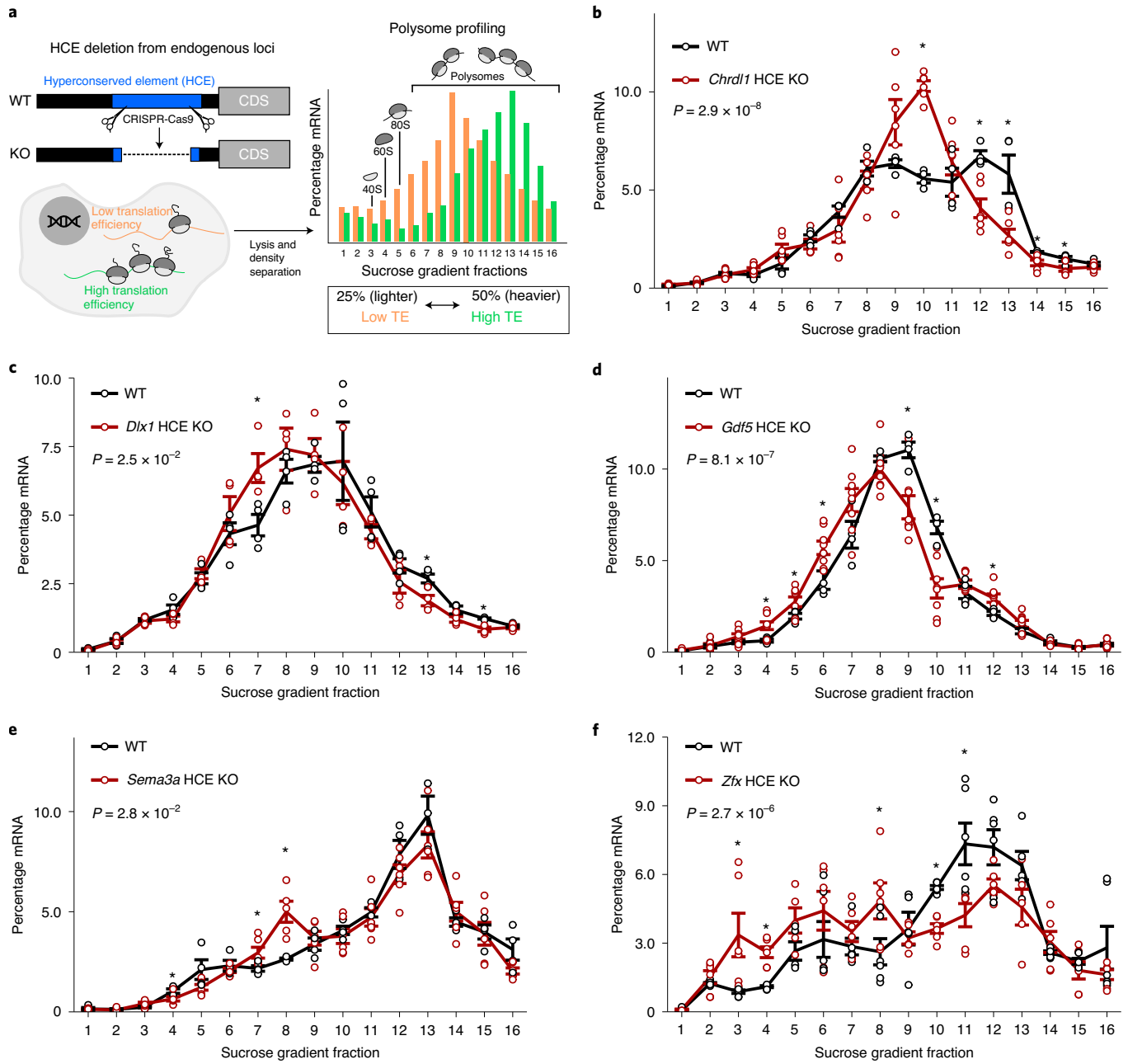

Fig. 2 | Hyperconserved 5′ UTRs impact translation efficiency. a, Schematic of experimental design for testing the impact of hyperconserved 5′ UTRs on translation of coding genes. Shift in the distribution of the mRNAs across sucrose gradient fractions towards the right (heavier polysomes) indicates more average ribosome loading and higher translation efficiency (TE), while shift towards the left indicates lower translation efficiency. **b**–**f**, Polysome profiles of wild type versus hyperconserved element (HCE) knockout cells for *Chrd1* (**b**), *Dlx1* (**c**), *Gdf5* (**d**), *Sema3a* (**e**) and *Zfx* (**f**). Distribution of mRNAs across sucrose gradient fractions are plotted. The *y* axis (the line) plots the mean percentage mRNA for each fraction. Error bars indicate standard error. Asterisk indicates two-sided *t*-test $P \leq 0.05$ for each fraction between the knockout and the wild type, $n = 4$. Indicated *P* value is calculated by Fisher's method across all fractions.

PhastCons elements within the h5UTRs as 5′ UTR hyperconserved elements (HCEs).

We next asked if h5UTRs are more likely to be discordant in their mRNA:protein expression levels, which would suggest post-transcriptional regulation. Using the GTEx Consortium tissue-specific transcriptomics and proteomics dataset, we determined if genes with h5UTRs have a different distribution of per-gene cross-tissue correlations in mRNA versus protein levels, compared to genes with similarly sized, nonconserved (defined as no overlap with LOD ≥ 500 PhastCons elements) 5′ UTRs[27,28]. For 181 h5UTR genes, both RNA and protein expression were detectable in at least ten tissues and the h5UTRs were annotated in both human and mouse RefSeq databases. Compared to all genes or to size-matched nonconserved controls, we observe significantly lower (Wilcoxon rank-sum test $P = 0.0013$, $P = 0.0017$, respectively) cross-tissue correlations (Pearson) for h5UTR genes (Fig. 1b). We also compared cross-tissue correlations of h5UTR genes with RNA variance-matched nonconserved controls to eliminate a model in

which h5UTRs impact the correlations only through a different dynamic range of variation in RNA expression. The correlations were still lower for the h5UTR group ($P=0.03$) (Extended Data Fig. 1d). Alternative 5′ UTR isoforms are also more frequently annotated for genes with h5UTRs than for all genes or nonconserved controls (Extended Data Fig. 1e). In summary, protein levels of h5UTR genes, as a group, are more difficult to predict with RNA levels alone than those of nonconserved 5′ UTR genes, suggesting that extreme sequence conservation in the 5′ UTR may be due to tissue-specific post-transcriptional control.

To describe the potential biological functions of genes with h5UTRs, we surveyed gene ontology (GO) terms enriched in the h5UTR gene set. To ensure the specificity of the enrichment, we also analyzed a length-matched set of nonconserved 5′ UTR genes, which did not yield any enriched term (Extended Data Fig. 1f). h5UTR GO terms highlighted genes critical for vertebrate embryonic developmental processes (Fig. 1c,d and Supplementary Table 2). For example, h5UTR genes are involved in morphogenesis of major tissues and organs, especially the nervous system. Genes that are part of signaling pathways involving the molecules WNT, retinoic acid, GABA, FGF, activin, BMP, PDGF, Notch, VEGF, hedgehog or Semaphorins are also abundantly present. We also note the genes involved in epigenetics, such as chromatin remodeling and histone acetylation. Additionally, when we intersected known disease-associated variants with h5UTRs, we identified five potentially interesting associations, which suggest that these regions may also play a functional role in disease (Supplementary Table 3)[29]. Overall, these annotation enrichments suggest that h5UTRs may play an important role in the post-transcriptional control of core embryonic developmental regulators.

Hyperconserved 5′ UTRs impact translation efficiency. To address experimentally whether the h5UTRs could impact the translational efficiency of mRNAs, we chose five candidates (*Chrdl1*, *Gdf5*, *Dlx1*, *Sema3a* and *Zfx*) that function in contexts where spatiotemporal expression patterns are important for embryonic development. Chrdl1 is a bone morphogenetic protein (BMP) antagonist with numerous functional roles in cell differentiation and synapse plasticity, and is implicated in multiple neurological disorders[30–35]. Gdf5 is a transforming growth factor (TGF)-β family protein with roles in skeletal and nervous system development[36–39]. Dlx1 is a homeobox transcription factor that has critical roles in craniofacial patterning, as well as in the differentiation and survival of neurons in the brain[40,41]. Sema3a is a semaphorin family protein that is secreted and functions as a guidance cue for axons and vasculatures[42–46]. Zfx is an X-linked transcription factor protein that regulates self-renewal of embryonic and hematopoietic stem cells[47].

To examine the contribution of h5UTRs, we introduced deletions into the 5′ UTRs of *Chrdl1*, *Gdf5*, *Dlx1*, *Sema3a* and *Zfx* using pairs of CRISPR–Cas9 single guide RNAs (sgRNAs) targeting segments ranging between 50 and 200 nucleotides within the HCEs (Supplementary Figs. 2–6 and Supplementary Table 4). We used either mouse embryonic stem cells (mESCs), mESCs treated with retinoic acid to promote differentiation or NIH3T3 cells, reflecting the cell types and conditions where these transcripts are expressed for analysis of translation (Supplementary Fig. 1a). Polysome profiling allows quantification of translational efficiency independent from effects on transcript levels (Fig. 2a). The mRNAs that are more highly translated are expected to be present in heavier polysomes as they are bound by more ribosomes. As expected, global translation levels displayed no difference between the wild types and CRISPR–Cas9-mediated HCE knockout cells (Supplementary Fig. 1b–f). However, we observe that, for all five candidates tested, the deletion mutants exhibited a shift in the distribution of the targeted mRNA species from the heavier polysomes into the lighter polysomes, indicating a decrease in translation efficiency (Fig. 2b–f). These findings suggest that h5UTRs may frequently harbor uncharacterized, additional *cis*-enhancers of translation initiation.

Noncanonical translation enhancer in hyperconserved 5′ UTRs. There has been growing evidence for the importance of less understood, alternative mechanisms of initiation independent of the cap-eIF4E interaction, which have the potential for enhancing transcript-specific regulation of gene expression[25,48–53]. For example, it has been estimated that 5–10% of cellular mRNAs may undergo cap-independent translation[54,55]. The HCE of *Hoxa9* contains a functional RNA element previously shown to direct translation initiation in a cap-independent manner, which is required for proper embryonic development[25]. Therefore, we asked whether other h5UTRs can similarly activate noncanonical translation initiation.

To test this hypothesis, we performed a large-scale reporter assay to measure the levels of noncanonical translation initiation from the h5UTRs. We synthesized and cloned a library of 253 full-length h5UTRs into a bicistronic reporter construct, containing two reporter genes, *Renilla* and firefly luciferase, that are transcribed as one mRNA. The first cistron, *Renilla* luciferase, is positioned immediately downstream of the promoter and is translated by cap-dependent translation. The second cistron, firefly

Fig. 3 | Noncanonical translation enhancer in hyperconserved 5′ UTRs. a, Measurement of noncanonical translation initiation activity from 253 hyperconserved 5′ UTRs by bicistronic reporter assay. Each dot is a 5′ UTR, where the *x* axis is the maximum luciferase reporter ratio across six different cell types, and the *y* axis is the rank of the reporter ratio from low to high. The skewing is reflective of the bimodal distribution of the activities (see also Extended Data Fig. 2a), and the color of the dot indicates estimated proportion of false positives on the basis of mixture modeling of two Gaussian distributions. The dashed line indicates the reporter ratio above which 10% of the hits are expected to be false positives. Genes labeled in red: HCV and EMCV are positive control viral IRES; others are select h5UTRs with annotated biological functions in embryonic development. **b**, Heat map of noncanonical translation initiation activity for 36 significantly varying h5UTRs across five indicated cell types (*F*-test, FDR ≤ 0.05). $n=4$ for C10T1/2, mESC and EB; $n=6$ for NSCs, neurons, limb mesenchyme culture. The color shows row *z*-scaled mean $\log_2$ reporter activities. The 5′ UTRs are ordered by clustering similar reporter activity patterns across cell types. **c**, Violin plot of bicistronic reporter activities from hyperconserved and nonconserved 5′ UTRs in 10T1/2 cells. *P* indicates the two-sided Wilcoxon rank-sum test *P* value. Box hinges: 25% quantile, median, 75% quantile, respectively, from left to right. Whiskers: lower or upper hinge ±1.5 × interquartile range. **d**, The effect of various truncations of the h5UTRs on noncanonical initiation and total translation efficiency. Also see Extended Data Fig. 3b. Positions of truncations. Dashed lines indicate truncations and bars indicate the remaining sequences. Purple horizontal lines within bars indicate uORFs (left). Noncanonical initiation efficiency (middle). Total translation efficiency (right). The *x* axis indicates the geometric mean of luciferase reporter ratios relative to the wild type. Error bars indicate geometric standard error. Dashed line marks the reporter ratio for the wild-type 5′ UTR. Asterisk indicates two-sided *t*-test $P \leq 0.05$ for each truncation mutant versus the full-length wild type. The numbers to the left of the bars indicate exact *n* and *P* values for each comparison versus the full length. **e**, Comparison of translational activities between the full-length h5UTR versus only the first 300 nucleotides of the h5UTR. A total of 38 different pairs are tested. The *x* axis indicates the mean $\log_2$ luciferase reporter ratios of each truncation relative to its full-length wild type. Error bars indicate standard error of the $\log_2$ luciferase activity ratios. Bars colored in red indicate significantly reduced translation in the shorter, truncated 300-nucleotide fragment; black indicates significant increase (two-sided *t*-test, $P \leq 0.05$, paired $n=3$, marked by asterisk). The numbers to the left of the bars indicate exact *P* values for each comparison versus the full length.

luciferase, can only be efficiently translated if the intercistronic inserted sequence enhances noncanonical translation initiation. To perform the reporter assays, we initially selected the mouse 10T1/2 cell line, a mesodermal cell line, as a pilot cell type and further expanded our analysis to include other murine cell types (mESCs, neural stem cells (NSCs), embryoid bodies, neurons and primary cultures of limb bud mesenchyme) to better represent a repertoire of lineages and differentiation trajectories in the developing embryo, and to capture instances of cell-type-specific translation control.

We noticed two groups of reporter activities distributed in a bimodal distribution for each of the cell types (Extended Data Fig. 2a). Within the higher group, we found the three positive controls that we included in the reporter assays, which all promote cap-independent translation: hepatitis C virus (HCV) IRES, encephalomyocarditis virus (EMCV) IRES and the Hoxa9 h5UTR. The 'empty' negative control reporter activity is found in the lower group, near its median. Thus, the lower component appears to represent the background noise level present in our reporter assays.

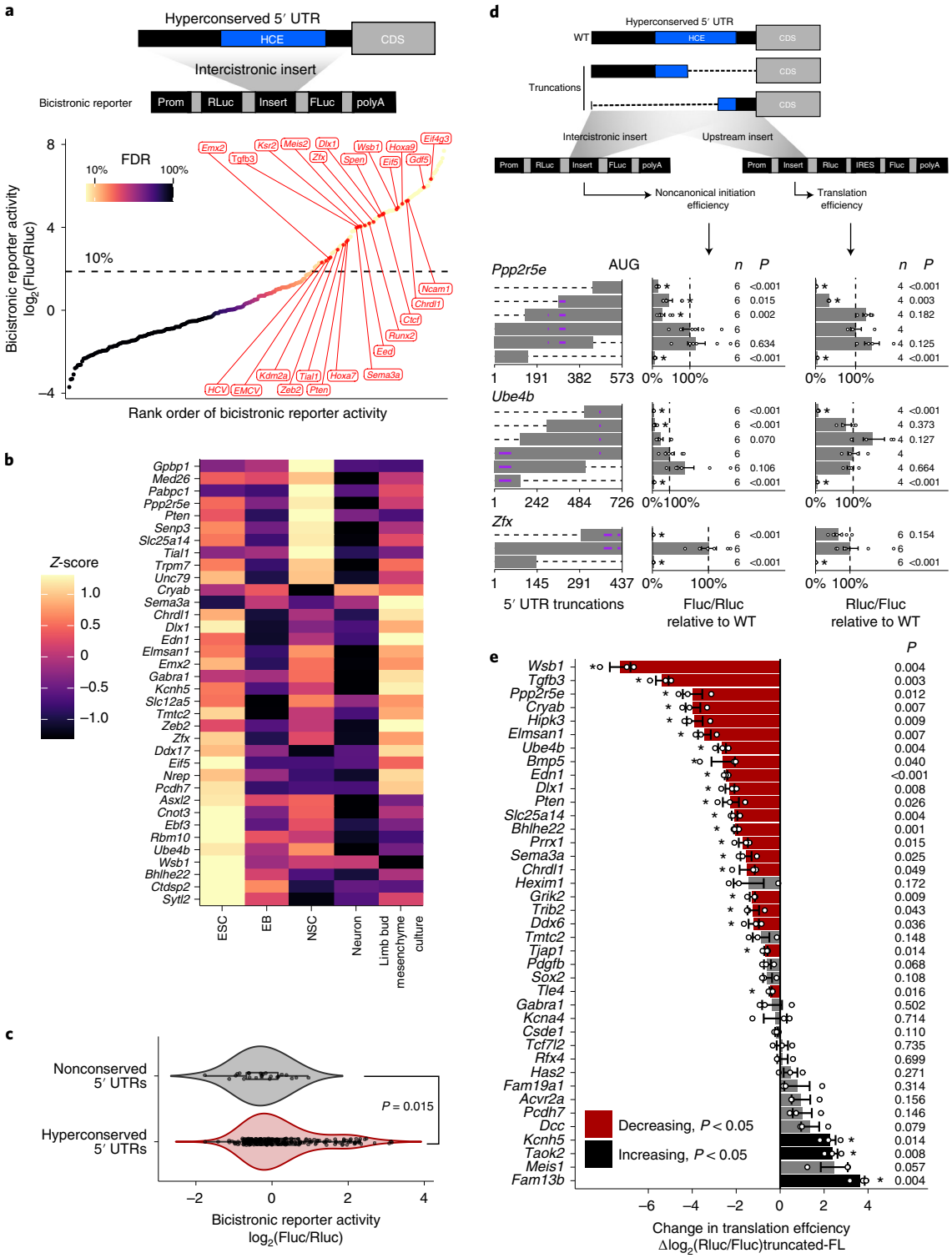

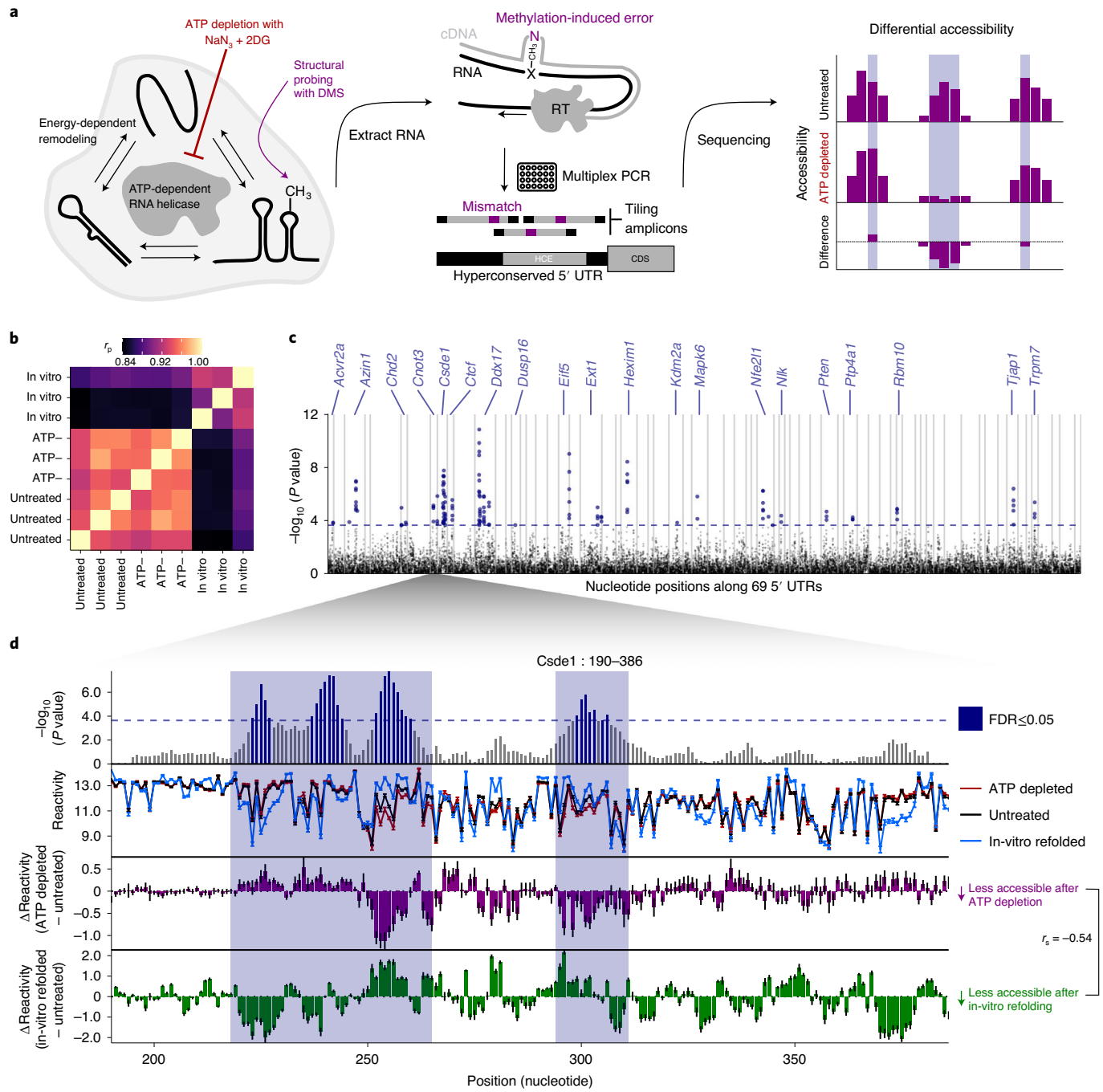

Fig. 4 | Cellular remodeling hyperconserved 5′ UTR RNA structures. a, Schematic of identifying RNA structures under cellular remodeling in h5UTRs. Multiplexed, targeted DMS chemical probing of 69 h5UTRs inside cells from their endogenous mRNAs is performed following ATP depletion treatment to stop RNA helicase activity. **b**, Heat map of correlation (Pearson's) matrix across replicate samples for untreated, ATP depleted and in vitro refolded samples (three each). The correlation values are calculated from a vector of normalized accessibility values for all nucleotides passing per-amplicon reproducibility cut-off. **c**, Manhattan plot of differential accessibility tests in 11-nucleotide overlapping windows across the 5′ UTRs. The *y* axis indicates $-\log_{10}$ (KS test *P* value) for each window along 69 5′ UTRs in the *x* axis. Dashed line indicates the *P* value cut-off at which permutation FDR is at 5%. **d**, Enlarged view of differential accessibilities along the *Csde1* 5′ UTR from positions 190 to 386. Top plot shows $-\log_{10}$ (*P* value) for each window. Highlighted boxes mark significantly different windows, above the dashed line indicating 5% FDR. Middle plot shows differential accessibility on the *y* axis, where greater than zero indicates increased accessibility upon ATP depletion and less than zero indicates decreased accessibility. Bottom plot shows differential accessibility for in-cell versus in vitro refolded RNA. Error bars in each plot show standard error, $n = 3$.

Using mixture modeling of the bimodal distribution, we estimated the false discovery rate (FDR) for each tested h5UTR as the probability that the reporter activity of the tested h5UTR could have come from the lower noise group. Using the maximum reporter activity across all six assayed cell types, we estimated that the proportion of the tested h5UTRs with noncanonical initiation activity is 33%. At 10% FDR, we are able to identify 90 h5UTRs with high noncanonical translation activity in at least one cell type (Fig. 3a

and Supplementary Table 5). Of the 90 5′ UTRs with noncanonical translation activity, two are previously known from the literature[56,57]. The five genes (*Chrdl1*, *Gdf5*, *Dlx1*, *Sema3a*, *Zfx*) for which we demonstrated evidence of translational enhancers (Fig. 2a–f) fall into this class of 5′ UTRs promoting noncanonical translation initiation. We observe that for 36 of the 5′ UTRs, their reporter activities are significantly variable across the different primary cell types that we tested (Fig. 3b). Additionally, to examine whether cell-type-specific noncanonical translation may be relevant in an endogenous context, we compared the polysome profiles of h5UTRs that show increased bicistronic reporter activity in NSCs relative to mESCs. Of the nine h5UTRs analyzed, five (*Gpbp1*, *Ppp2r5e*, *Pten*, *Trpm7*, *Senp3*) showed shifts that indicated significant increase in translation in NSCs over mESCs, despite lower global translation in NSCs compared to mESCs (Extended Data Fig. 2b–l). These results suggest that noncanonical translation initiation mediated by h5UTRs could be controlled in a highly regulatable fashion across different cell types.

We determined that the higher reporter ratios are not due to cryptic transcriptional and splicing effects, since the ratios of the mRNA levels of the two luciferase genes measured by quantitative PCR (qPCR) in transfected cells are not skewed or correlated with ratios of the two luciferase reporter activities (Extended Data Fig. 3a). In addition, we selected 23 nonconserved mouse 5′ UTR sequences and tested their activities in 10T1/2 cells. The distribution of nonconserved 5′ UTRs was unimodal near the lower noise component of the mixture observed for the conserved set (Wilcoxon rank-sum test $P=0.015$; Fig. 3c). This result further indicates that the extreme conservation in the 5′ UTRs enriches for noncanonical translation initiation, suggesting their predictive value in identifying such elements genome wide.

It has often been argued that cap-independent translation typically makes only a minimal contribution to overall translation efficiency, except under conditions during which cap-dependent translation is globally reduced[58–60]. To understand the contribution of the noncanonical translation activation by the h5UTRs, we performed two different reporter assays with a series of truncated h5UTRs. The first reporter assay was the bicistronic reporter assay, as described above. In the second reporter assay, the endogenous capped monocistronic *Renilla* luciferase was employed to measure total translational levels for truncated h5UTRs where cap-dependent translation is active. For 9 out of 11 h5UTR truncations in the two reporters transfected to 10T1/2 cells, we observed that at least one truncation significantly reduced noncanonical initiation, as well as the total translational levels (Fig. 3d and Extended Data Fig. 3b). The trend for truncations to frequently reduce total translation activity is notable, since cap-dependent translation initiation typically increases in efficiency when the 5′ UTR is shortened. We asked if this is more generally true in a larger set of 38 h5UTRs by comparing the total translation directed by the full length versus only the first 300 nucleotides of the h5UTR, without a large proportion of the HCE in each h5UTR. Of the 38 h5UTRs, 20 decrease significantly in the shorter truncated 5′ UTR relative to the full length, while only 5 increase significantly (Fig. 3e). In contrast, truncating long, nonconserved 5′ UTRs does not show the same trend for decreased translation (Extended Data Fig. 3c,d). Furthermore, there is no correlation between the change in the density of upstream AUGs and the change in reporter activities (Extended Data Fig. 3e). Taken together, noncanonical translation enhancer elements in h5UTRs widely impact total translation efficiency in physiological cellular conditions, suggesting that h5UTR genes may be translated via more specialized initiation mechanisms that utilize evolutionarily constrained, sequence-specific *cis*-regulatory features.

Cellular remodeling of hyperconserved 5′ UTR RNA structures. Higher order structures are inherent features of RNA molecules that underpin their biochemical function. The majority of previous covariation-based predictions of RNA structures in vertebrates occur in 'moderately' conserved regions of the genome and miss the HCEs[61–64]. This is because covariation analysis requires not only sufficient conservation for alignment, but also sufficient variation for statistical power[65,66]. Since extreme conservation limits the extent to which covariation signals can be informative, addressing this question currently requires additional experimental data.

We postulated that specific regions of mRNA that display localized sensitivity in their structures to active cellular remodeling by RNA helicases could potentially lead us to functionally relevant structures within h5UTRs that guide translation initiation. To obtain high coverage accessibility data for a large number of h5UTRs, we initially performed a highly multiplexed amplicon sequencing adaptation of dimethyl sulfate (DMS) mutational profiling[67–69]. DMS profiling was performed in mESCs under the conditions of no treatment or depletion of ATP to eliminate helicase

Fig. 5 | icM² reveals structured elements in the hyperconserved *Csde1* 5′ UTR. a, Schematic of localized perturbation patterns that may be observed in M² data. Here, the mutant does not disrupt the overall structure and 'releases' its base-pairing partner. This results in an increase of chemical accessibility signal at the interacting nucleotide. Systematic profiling of accessibilities by M² results in an array of such mutant accessibility data into an approximate contact map. **b**, Schematic of global rearrangement patterns that may be observed in M² data. Here, multiple conformations of the RNA molecule are present together in an ensemble at nonnegligible relative proportions. Mutations can shift this balance, such that one structural state is favored over the other. In this case, M² reveals large-scale accessibility perturbations across a longer stretch of the RNA molecule. Multiple mutations often impact the relative proportions in similar ways, which manifests as correlated arrays accessibility changes in the M² data matrix. **c**, Schematic of the icM² method. Mutagenesis library of the target RNA of interest is first generated using error-prone PCR followed by cloning into an expression vector. The cells are transfected with the library and treated with DMS. Total RNAs are extracted. Read-through reverse transcription encodes DMS-modified nucleotides as mutations on the cDNA, which are read out by high-throughput sequencing. Correlated mutations in sequencing reads are then quantified and the resultant covariation matrix is analyzed for signature perturbation patterns. **d**, Heat map of icM² accessibility matrix for *Csde1* 5′ UTR from position 190 to 386. For each row, the chemical mapping profile of a single-nucleotide variant of the RNA is plotted across the columns, where the colors indicate *z*-scaled accessibility change values from the wild-type RNA. One-dimensional data from each mutant are vertically stacked to display a two-dimensional matrix. White boxes mark the two regions (A: positions 334–363 and B: positions 215–315) that display strong perturbation signals, which reveal their structures. **e**, A structure model (structure W) of region A. Bases colored in red indicate mutations with accessibility changes observed in icM² data that are consistent with the model. **f**, Scatter plot showing correlations of per-nucleotide accessibilities between each mutant versus the 'wild type' (wild-type accessibilities are not directly measured, but mean accessibilities of 10 lowest variable mutants are used as a close approximation) on the *y* axis and nucleotide positions along the *x* axis. *P* indicates two-sided Wilcoxon rank-sum test *P* value for the difference in distributions of correlations between region B versus other nucleotides. **g**, Multiple species alignment for *Csde1* 5′ UTR from position 125 to 548. For each row, the sequence alignment of a species is plotted across the columns, where the colors indicate match/substitution/insertion/deletion at each nucleotide. The alignment positions are relative to the mouse sequence. The top row is the mouse alignment, colored separately from other rows as a reference to indicate the identity of the bases in each position in the multiple species alignment.

activity (Fig. 4a,b). We successfully profiled 161 tiling amplicons of 250 nucleotides in size across 69 endogenously expressed h5UTRs. We identified 140 11-nucelotide windows over 20 h5UTRs that were significantly different (FDR ≤ 0.05) between ATP depletion and no treatment (Fig. 4c and Supplementary Table 6). One known source of RNA structure remodeling in the cell is ribosome unwinding of mRNAs during translation, and thus the presence of upstream open reading frames (uORFs) may lead to differential accessibilities

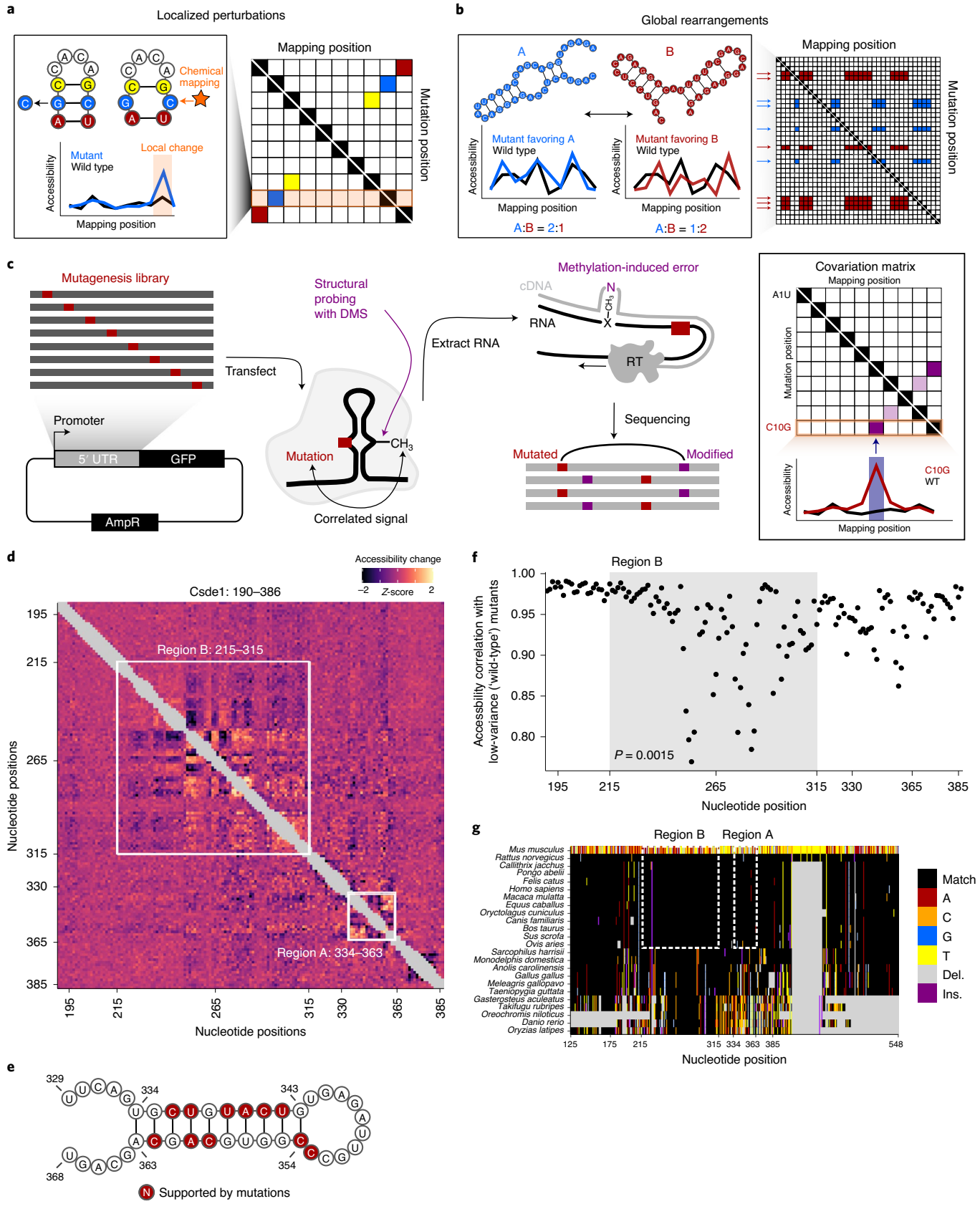

upon ATP depletion[70]. We tested whether differential accessibility windows (FDR ≤ 0.05) are over-represented in upstream AUGs or potential uORFs, but did not observe significant enrichment for either case, arguing against this possibility (Extended Data Fig. 4a,b). Together, these results suggest the frequent presence of secondary structures under active energy-dependent cellular remodeling within h5UTRs.

For the 20 significant h5UTRs with ATP-dependent differential accessibility, we found strong enrichment of mammalian phenotype ontology terms that indicate essential early developmental gene function: 16 out of the 20 were annotated for either embryonic or neonatal lethality (Supplementary Table 7). We also found known associations with human genetic diseases for 6 out of the 20 (Supplementary Table 8). This suggests that the extremely conserved, structured RNA elements could be impacting post-transcriptional regulation of key developmental genes.

Among the most striking patterns of ATP-dependent differential accessibility observed is the 5′ UTR of *Csde1*, also known as upstream of N-ras (Unr). *Csde1* encodes an RNA-binding protein (RBP) that regulates translation and stability of its target mRNAs. It is known to impact cell cycle, stem cell differentiation, apoptosis and dosage compensation[71–77]. *Csde1* is implicated in a variety of human diseases, including Diamond–Blackfan anemia, autism spectrum disorders and cancers[78–81]. We identified a 150-bp stretch from positions 215 to 365 encompassing an HCE that shows large-scale accessibility changes upon ATP depletion (Fig. 4d). Notably, the accessibility changes observed in the *Csde1* h5UTR following ATP depletion are different from the changes observed between in-cell and in vitro refolded RNA; there is even a slight negative correlation ($r_s = -0.54$). Such discordance is also observed in a number of other h5UTRs with ATP-dependent differential accessibility (Extended Data Fig. 4c). Thus, active remodeling by RNA helicases can be important for the formation of cellular structures distinct from those formed under in vitro conditions.

***Csde1* 5′ UTR encodes alternative functional RNA structures.** As a model to investigate cellular RNA structure and its remodeling in HCEs, we sought to further characterize the helicase-sensitive structures in the *Csde1* h5UTR. In particular, we developed in-cell mutate-and-map (icM^2), a powerful methodology that enables application of the M^2 strategy, wherein systematic mutagenesis of RNA is coupled with chemical mapping to generate accessibility profiles for every mutated nucleotide, inside the native cellular context (Fig. 5a–c)[82]. In icM^2, the target sequence of interest is mutagenized using error-prone PCR, cloned as a pool into an expression plasmid and transfected into cells. Following the treatment of transfected cells with DMS, total RNAs are extracted and subjected to read-through reverse transcription, where modified nucleotides are misincorporated as mutations on the complementary DNA, which are amplified and sequenced. Correlated mutations in sequencing reads are then quantified, and the resultant covariation matrix is analyzed for signature perturbation patterns. icM^2 is particularly suited for analysis of h5UTRs, as it directly addresses what RNA structural changes occur if each of the extremely conserved nucleotides is mutated during evolution.

We applied icM^2 in three windows tiling across the *Csde1* 5′ UTR in mESCs. We observed strong perturbation signals in the 215–365 positions along the 5′ UTR, where we had originally observed large differential accessibilities in response to elimination of RNA helicase unwinding activities (Fig. 5d). The visualization of the icM^2 accessibility matrix immediately highlighted two subregions. The first region is around positions 334–363 (region A), where short-range localized perturbations indicated the presence of a small stem loop motif. Here, the data corresponded well to the expected accessibility changes for the lowest free energy structure (structure W) predicted for the region (Fig. 5e). The second region is around positions 215–315 (region B), where correlated global perturbations across a long stretch of about 100 nucleotides indicated the presence of multiple conformations. Remarkably, these correlated global perturbations occur for almost every mutation across the 100-nucleotide stretch, revealing the strong sensitivity of the ensemble state to the precise sequence identity of each base. This is highlighted by the correlations of per-nucleotide accessibilities between each mutant versus the 'wild type' (Fig. 5f; Wilcoxon rank-sum test $P = 0.0015$ for mutants in region B versus other mutants). Therefore, at least two conformational states exist whose relative proportions inside the cell are affected by a mutation in almost any of the extremely conserved nucleotides. In addition, we observe the strongest conservation signal of the *Csde1* 5′ UTR in region B, where, amongst placental mammals, there is near-perfect sequence identity (Fig. 5g). These results suggest a structural explanation for why such extreme conservation levels may be required. Furthermore, examining the conservation levels and ATP-dependent accessibility profiles across all other h5UTRs reveals that the average per-nucleotide conservation levels in significantly differential accessibility regions (FDR ≤ 0.05) display exceedingly high conservation levels compared to the rest of the RNA (Extended Data Fig. 5a,b). Thus, encoding of actively remodeled cellular RNA structures may be a broadly occurring phenomenon associated with the extreme conservation levels in h5UTRs.

We next asked what candidate structures might explain the observed alternative states of the ensemble in region B. We used the average accessibility change profiles for the two clusters as two separate constraints for RNA folding (Fig. 6a). Constraining by the cluster 1 average accessibility profile revealed a well-defined conformation (structure X) disrupted by cluster 1 mutants in the

Fig. 6 | *Csde1* 5′ UTR tunes translation efficiency by encoding multiple alternative structures that are actively maintained by RNA helicases. **a**, Multidimensional scaling (MDS) plot showing dimensionality reduction ($K = 2$) of icM^2 data matrix (positions 190–386). Dots indicate each single-nucleotide variant of the RNA, where the colors/annotations mark the mutants grouped into two clusters, determined heuristically by visual inspection of the positions on the plot. **b**–**d**, Structure models (X (**b**), Y (**c**), Z (**d**)) for the alternative conformations in region B. Bases colored in red or blue indicate mutations with similar patterns of accessibility changes grouped into two clusters as shown in **a**. Yellow outline indicates mutants that are also tested for function in luciferase reporter assay (shown in **g**). Percentages indicate relative proportions of the three structures estimated by REEFFIT. **e**, REEFFIT estimates of the mixing proportions (relative to the maximal amount of change that can be observed by the single mutations) for structures X,Y, Z upon introduction of single-nucleotide mutations. The *y* axis indicates the stacked bars indicating proportions, along the variants from the two clusters in the *x* axis. **f**, Comparison of average accessibility changes for each of the two clusters with accessibility changes observed upon ATP depletion at region B. Top plot shows the reactivity differences upon ATP depletion, where greater than zero indicates increased accessibility upon ATP depletion and vice versa. Middle and bottom plots show the cluster average accessibility change *z*-scores. Spearman correlation between cluster 1 and ATP depletion is 0.83 and −0.8 between cluster 2 and ATP depletion. **g**, The effect of shifting the relative balance of the alternative conformations at region B on translation. The *y* axis shows changes in luciferase reporter activities compared to the wild-type (WT) sequence when the single variants affecting mixing proportions (shown in **e**) are introduced into the full-length *Csde1* 5′ UTR upstream of the luciferase reporter. Plotted are the mean; error bars indicate standard error. The bars and labels along *x* axis are colored according to whether they are wild type, cluster 1 mutants or cluster 2 mutants. Dashed line indicates the wild-type luciferase reporter level. Asterisk indicates a significant difference between each mutant and wild type (two-sided *t*-test $P \leq 0.05$, $n = 3$).

helices and stabilized by cluster 2 mutants in the loops (Fig. 6b). Constraining by the cluster 2 profile resulted in a higher entropy fold, which was nevertheless readily visualizable by two representative medoid conformations (structures Y and Z; Fig. 6c,d). To estimate the relative mixing ratios of these structures, we chose to apply the RNA ensemble extraction from footprinting insights technique (REEFFIT)[83]. For the wild-type sequence, REEFFIT yielded proportions of 67±9%:10±4%:23±9% for the representative structures X, Y and Z, respectively (Fig. 6b–d). It also predicted how these proportions are expected to change across the individual mutants, adding quantitative estimates to our initially qualitative observations of alternative structural states. For example, cluster 1 mutants disrupt structure X to favor structures Y and Z, changing the relative proportions of X:Y:Z to 30%:13%:57% on average, while cluster 2 mutants act in the opposite direction, shifting the proportions to 91%:6%:3% (Fig. 6e). We further discovered that the accessibility change profiles of the two clusters of mutants are closely correlated with helicase-dependent accessibility change (Fig. 6). This observation suggests that elimination of RNA helicase unwinding activity decreases the proportion of structure X in the cell and does so to

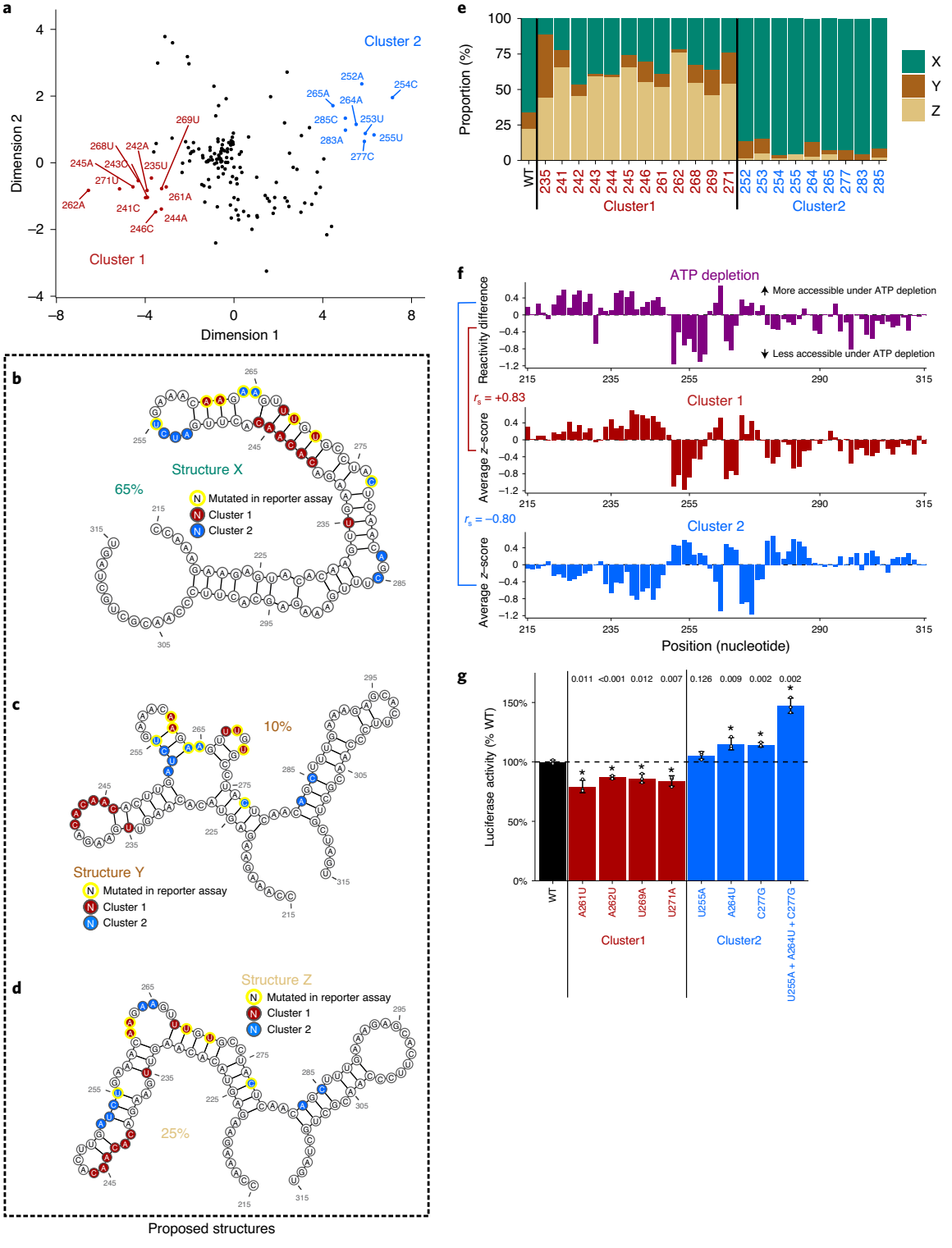

increase the fraction of the alternative structures Y and Z. Notably, structure X has multiple long stems (positions 232–282); that is, the helicase activity promotes a low free energy structure and potentially may act as a chaperone[84]. It is formally possible for other direct contacts on the exact methylation sites of the nucleotides, such as a direct RBP interaction on the base-pairing face, to produce localized 'footprints' on the accessibility profiles; however, this would not drastically impact our model. Taken together, we propose three candidate conformations to account for our icM^2 signal observed in region B of the *Csde1* 5′ UTR and hypothesize that the cell is actively expending energy to maintain the precise relative balance of these conformations in the cellular structural ensemble.

In our initial one-dimensional DMS profiling analysis of h5UTRs in mESCs, we had observed that the accessibility profiles of many RNAs refolded in vitro were discordant from those of RNAs in cells (Fig. 4d and Extended Data Fig. 5c). To further expand on these differences and to actually compare in-cell versus in vitro RNA structures, we also performed in vitro M^2 on *Csde1* h5UTR. We observed a strikingly different accessibility matrix (Extended Data Fig. 6a,b). These results highlight the importance of resolving flexible conformations that can occur uniquely under cellular conditions.

Lastly, we asked whether such a shift in the balance of structural conformations has a functional consequence on the translation of the downstream gene. We performed luciferase reporter assays with mutant *Csde1* 5′ UTRs carrying a number of substitutions from each of the two clusters, which are predicted to change the relative proportions. We selected four different nucleotide positions from cluster 1 and three from cluster 2, hypothesizing that similar patterns of expression level changes may be observed among each cluster. We observed that all cluster 1 mutants decreased firefly luciferase activities by 15–20% compared to the wild-type 5′ UTR (Fig. 6g). In contrast, cluster 2 mutants increased the reporter activities by 5–15%. When the three individual single mutations from cluster 2 are combined, the effect size is increased to about 50%. The dynamic range of final protein levels can thus be tuned according to the relative proportions of the multiple conformations along the RNA structural landscape of the *Csde1* 5′ UTR. Together, these results suggest that the exact proportions and properties of the RNA structural ensemble are a critical functional requirement under negative selection in hyperconserved vertebrate 5′ UTRs.

Discussion

Extreme sequence conservation has long been observed in noncoding regions of vertebrate genomes, yet our current functional knowledge of these elements falls short in explaining why and how such conservation levels exist. Here, we uncover a functional role for hyperconserved 5′ UTRs in regulation of translation and report their unexpected enrichment in noncanonical initiation sites, particularly within those transcripts critical for development in vertebrate species. We speculate that there may potentially be many different types of unknown noncanonical mechanisms that are adopted by these 5′ UTRs and that further investigations may identify new classes of RNA elements that accommodate more specialized mechanisms of translational control. The activities of h5UTRs may vary across cells and tissues, which may result in differential translatability of these mRNAs.

A crucial component of decoding *cis*-regulatory features at the level of RNAs is the determination of their higher order structure beyond the primary sequence. To this end, we developed a technique, icM^2, to examine the RNA structural ensemble within cells. We found that cells precisely tune protein expression levels by remodeling the hyperconserved *Csde1* 5′ UTR to maintain the relative proportions of multiple functional conformations. While icM^2 revealed a highly dense array of mutations that disrupt such an actively enforced balance of dynamic structures in the *Csde1* 5′ UTR across a ~100-nucelotide-long stretch, the same mutations are negatively selected against in nature across vertebrate species. This suggests that selective pressures for translational regulation can lead to extreme sequence constraints when an ensemble of multiple functional conformations must be encoded over a single stable structure to ensure a dynamic range of translational outputs. The observation that regions of h5UTRs under helicase-dependent structural remodeling in general display the highest conservation levels further suggests that a similar phenomenon could extend more broadly to other h5UTRs and may, at least in part, explain extreme conservation in 5′ UTRs at the level of RNA.

Flexible structural states can potentially endow multiple functional states in regulatory elements that respond to environmental or cellular cues. Most current genome-wide efforts to identify functional structures have focused on single stable conformations. Our results underscore the necessity of the ensemble perspective of RNA structure in understanding the cellular activities of regulatory RNAs and the potential utility of extreme conservation in detecting such dynamically structured elements in the untranslated regions of mRNAs. We envision that hyperconserved 5′ UTRs will aid the discovery of functional RNA structures in vertebrate genomes and advance our broader understanding of post-transcriptional gene regulation in development, disease and evolution.

Online content

Any methods, additional references, Nature Research reporting summaries, source data, extended data, supplementary information, acknowledgements, peer review information; details of author contributions and competing interests; and statements of data and code availability are available at https://doi.org/10.1038/s41588-021-00830-1.

Received: 10 July 2020; Accepted: 26 February 2021;
Published online: 05 April 2021

References

1. Dermitzakis, E. T., Reymond, A. & Antonarakis, S. E. Conserved non-genic sequences – an unexpected feature of mammalian genomes. *Nat. Rev. Genet.* **6**, 151–157 (2005).
2. Harmston, N., Baresic, A. & Lenhard, B. The mystery of extreme non-coding conservation. *Philos. Trans. R. Soc. Lond. B. Biol. Sci.* **368**, 20130021 (2013).
3. Halligan, D. L. et al. Positive and negative selection in murine ultraconserved noncoding elements. *Mol. Biol. Evol.* **28**, 2651–2660 (2011).
4. Bejerano, G. et al. Ultraconserved elements in the human genome. *Science* **304**, 1321–1325 (2004).
5. Dimitrieva, S. & Bucher, P. Genomic context analysis reveals dense interaction network between vertebrate ultraconserved non-coding elements. *Bioinformatics* **28**, i395–i401 (2012).
6. Boffelli, D., Nobrega, M. A. & Rubin, E. M. Comparative genomics at the vertebrate extremes. *Nat. Rev. Genet.* **5**, 456–465 (2004).
7. Lindblad-Toh, K. et al. Genome sequence, comparative analysis and haplotype structure of the domestic dog. *Nature* **438**, 803–819 (2005).
8. Sandelin, A. et al. Arrays of ultraconserved non-coding regions span the loci of key developmental genes in vertebrate genomes. *BMC Genomics* **5**, 99 (2004).
9. de la Calle-Mustienes, E. et al. A functional survey of the enhancer activity of conserved non-coding sequences from vertebrate Iroquois cluster gene deserts. *Genome Res.* **15**, 1061–1072 (2005).
10. Sakuraba, Y. et al. Identification and characterization of new long conserved noncoding sequences in vertebrates. *Mamm. Genome* **19**, 703–712 (2008).
11. Dermitzakis, E. T. et al. Comparison of human chromosome 21 conserved nongenic sequences (CNGs) with the mouse and dog genomes shows that their selective constraint is independent of their genic environment. *Genome Res.* **14**, 852–859 (2004).
12. Katzman, S. et al. Human genome ultraconserved elements are ultraselected. *Science* **317**, 915 (2007).
13. Pennacchio, L. A. et al. In vivo enhancer analysis of human conserved non-coding sequences. *Nature* **444**, 499–502 (2006).
14. Visel, A. et al. Ultraconservation identifies a small subset of extremely constrained developmental enhancers. *Nat. Genet.* **40**, 158–160 (2008).
15. Visel, A. et al. A high-resolution enhancer atlas of the developing telencephalon. *Cell* **152**, 895–908 (2013).
16. Ahituv, N. et al. Deletion of ultraconserved elements yields viable mice. *PLoS Biol.* **5**, e234 (2007).

17. McLean, C. & Bejerano, G. Dispensability of mammalian DNA. *Genome Res.* **18**, 1743–1751 (2008).
18. Dickel, D. E. et al. Ultraconserved enhancers are required for normal development. *Cell* **172**, 491–499.e15 (2018).
19. Osterwalder, M. et al. Enhancer redundancy provides phenotypic robustness in mammalian development. *Nature* **554**, 239–243 (2018).
20. Lareau, L. F., Inada, M., Green, R. E., Wengrod, J. C. & Brenner, S. E. Unproductive splicing of SR genes associated with highly conserved and ultraconserved DNA elements. *Nature* **446**, 926–929 (2007).
21. Ni, J. Z. et al. Ultraconserved elements are associated with homeostatic control of splicing regulators by alternative splicing and nonsense-mediated decay. *Genes Dev.* **21**, 708–718 (2007).
22. Thomas, J. D. et al. RNA isoform screens uncover the essentiality and tumor-suppressor activity of ultraconserved poison exons. *Nat. Genet.* **52**, 84–94 (2020).
23. Calin, G. A. et al. Ultraconserved regions encoding ncRNAs are altered in human leukemias and carcinomas. *Cancer Cell* **12**, 215–229 (2007).
24. Liz, J. et al. Regulation of pri-miRNA processing by a long noncoding RNA transcribed from an ultraconserved region. *Mol. Cell* **55**, 138–147 (2014).
25. Xue, S. et al. RNA regulons in Hox 5′ UTRs confer ribosome specificity to gene regulation. *Nature* **517**, 33–38 (2015).
26. Siepel, A. et al. Evolutionarily conserved elements in vertebrate, insect, worm, and yeast genomes. *Genome Res.* **15**, 1034–1050 (2005).
27. Jiang, L. et al. A quantitative proteome map of the human body. *Cell* **183**, 269–283.e19 (2020).
28. GTEx Consortium. The GTEx Consortium atlas of genetic regulatory effects across human tissues. *Science* **369**, 1318–1330 (2020).
29. Steri, M., Idda, M. L., Whalen, M. B. & Orrù, V. Genetic variants in mRNA untranslated regions. *Wiley Interdiscip. Rev. RNA* **9**, e1474 (2018).
30. Blanco-Suarez, E., Liu, T.-F., Kopelevich, A. & Allen, N. J. Astrocyte-secreted chordin-like 1 drives synapse maturation and limits plasticity by increasing synaptic GluA2 AMPA receptors. *Neuron* **100**, 1116–1132.e13 (2018).
31. Sakuta, H. et al. Ventroptin: a BMP-4 antagonist expressed in a double-gradient pattern in the retina. *Science* **293**, 111–115 (2001).
32. Webb, T. R. et al. X-linked megalocornea caused by mutations in CHRDL1 identifies an essential role for ventroptin in anterior segment development. *Am. J. Hum. Genet.* **90**, 247–259 (2012).
33. Gandal, M. J. et al. Shared molecular neuropathology across major psychiatric disorders parallels polygenic overlap. *Science* **359**, 693–697 (2018).
34. Liu, T. et al. Chordin-like 1 improves osteogenesis of bone marrow mesenchymal stem cells through enhancing BMP4-SMAD pathway. *Front. Endocrinol.* **10**, 360 (2019).
35. Pei, Y.-F. et al. Hypermethylation of the CHRDL1 promoter induces proliferation and metastasis by activating Akt and Erk in gastric cancer. *Oncotarget* **8**, 23155–23166 (2017).
36. Osório, C. et al. Growth differentiation factor 5 is a key physiological regulator of dendrite growth during development. *Development* **140**, 4751–4762 (2013).
37. O'Keeffe, G. W. et al. Region-specific role of growth differentiation factor-5 in the establishment of sympathetic innervation. *Neural Dev.* **11**, 4 (2016).
38. Wu, H., Li, J., Xu, D., Zhang, Q. & Cui, T. Growth differentiation factor 5 improves neurogenesis and functional recovery in adult mouse hippocampus following traumatic brain injury. *Front. Neurol.* **9**, 592 (2018).
39. Buxton, P., Edwards, C., Archer, C. W. & Francis-West, P. Growth/differentiation factor-5 (GDF-5) and skeletal development. *J. Bone Joint Surg. Am.* **83-A**, S23–S30 (2001).
40. Panganiban, G. & Rubenstein, J. L. R. Developmental functions of the Distal-less/Dlx homeobox genes. *Development* **129**, 4371–4386 (2002).
41. Depew, M. J., Simpson, C. A., Morasso, M. & Rubenstein, J. L. R. Reassessing the Dlx code: the genetic regulation of branchial arch skeletal pattern and development. *J. Anat.* **207**, 501–561 (2005).
42. Polleux, F., Morrow, T. & Ghosh, A. Semaphorin 3A is a chemoattractant for cortical apical dendrites. *Nature* **404**, 567–573 (2000).
43. Serini, G. et al. Class 3 semaphorins control vascular morphogenesis by inhibiting integrin function. *Nature* **424**, 391–397 (2003).
44. Shelly, M. et al. Semaphorin 3A regulates neuronal polarization by suppressing axon formation and promoting dendrite growth. *Neuron* **71**, 433–446 (2011).
45. Polleux, F., Giger, R. J., Ginty, D. D., Kolodkin, A. L. & Ghosh, A. Patterning of cortical efferent projections by semaphorin–neuropilin interactions. *Science* **282**, 1904–1906 (1998).
46. Good, P. F. et al. A role for semaphorin 3A signaling in the degeneration of hippocampal neurons during Alzheimer's disease. *J. Neurochem.* **91**, 716–736 (2004).
47. Galan-Caridad, J. M. et al. Zfx controls the self-renewal of embryonic and hematopoietic stem cells. *Cell* **129**, 345–357 (2007).
48. Lee, A. S. Y., Kranzusch, P. J. & Cate, J. H. D. eIF3 targets cell-proliferation messenger RNAs for translational activation or repression. *Nature* **522**, 111–114 (2015).
49. Gilbert, W. V., Zhou, K., Butler, T. K. & Doudna, J. A. Cap-independent translation is required for starvation-induced differentiation in yeast. *Science* **317**, 1224–1227 (2007).
50. Martin, F. et al. Cap-assisted internal initiation of translation of histone H4. *Mol. Cell* **41**, 197–209 (2011).
51. Legnini, I. et al. Circ-ZNF609 is a circular RNA that can be translated and functions in myogenesis. *Mol. Cell* **66**, 22–37.e9 (2017).
52. Pamudurti, N. R. et al. Translation of circRNAs. *Mol. Cell* **66**, 9–21.e7 (2017).
53. Leppek, K. et al. Gene- and species-specific Hox mRNA translation by ribosome expansion segments. *Mol. Cell* **80**, 980–995.e13 (2020).
54. Hershey, J. W. B., Sonenberg, N. & Mathews, M. B. Principles of translational control: an overview. *Cold Spring Harb. Perspect. Biol.* **4**, a011528. (2012).
55. Weingarten-Gabbay, S. et al. Comparative genetics. Systematic discovery of cap-independent translation sequences in human and viral genomes. *Science* **351**, aad4939 (2016).
56. Xiao, Z.-S., Simpson, L. G. & Quarles, L. D. IRES-dependent translational control of Cbfa1/Runx2 expression. *J. Cell. Biochem.* **88**, 493–505 (2003).
57. Jang, G. M. et al. Structurally distinct elements mediate internal ribosome entry within the 5′-noncoding region of a voltage-gated potassium channel mRNA. *J. Biol. Chem.* **279**, 47419–47430 (2004).
58. Holcik, M. & Sonenberg, N. Translational control in stress and apoptosis. *Nat. Rev. Mol. Cell Biol.* **6**, 318–327 (2005).
59. El-Naggar, A. M. & Sorensen, P. H. Translational control of aberrant stress responses as a hallmark of cancer. *J. Pathol.* **244**, 650–666 (2018).
60. Spriggs, K. A., Bushell, M. & Willis, A. E. Translational regulation of gene expression during conditions of cell stress. *Mol. Cell* **40**, 228–237 (2010).
61. Washietl, S., Hofacker, I. L., Lukasser, M., Hüttenhofer, A. & Stadler, P. F. Mapping of conserved RNA secondary structures predicts thousands of functional noncoding RNAs in the human genome. *Nat. Biotechnol.* **23**, 1383–1390 (2005).
62. Torarinsson, E. et al. Comparative genomics beyond sequence-based alignments: RNA structures in the ENCODE regions. *Genome Res.* **18**, 242–251 (2008).
63. Parker, B. J. et al. New families of human regulatory RNA structures identified by comparative analysis of vertebrate genomes. *Genome Res.* **21**, 1929–1943 (2011).
64. Smith, M. A., Gesell, T., Stadler, P. F. & Mattick, J. S. Widespread purifying selection on RNA structure in mammals. *Nucleic Acids Res.* **41**, 8220–8236 (2013).
65. Eddy, S. R. Computational analysis of conserved RNA secondary structure in transcriptomes and genomes. *Annu. Rev. Biophys.* **43**, 433–456 (2014).
66. Rivas, E., Clements, J. & Eddy, S. R. Estimating the power of sequence covariation for detecting conserved RNA structure. *Bioinformatics* **36**, 3072–3076 (2020).
67. Homan, P. J. et al. Single-molecule correlated chemical probing of RNA. *Proc. Natl Acad. Sci. USA* **111**, 13858–13863 (2014).
68. Zubradt, M. et al. DMS-MaPseq for genome-wide or targeted RNA structure probing in vivo. *Nat. Methods* **14**, 75–82 (2017).
69. Mustoe, A. M., Lama, N. N., Irving, P. S., Olson, S. W. & Weeks, K. M. RNA base-pairing complexity in living cells visualized by correlated chemical probing. *Proc. Natl Acad. Sci. USA* **116**, 24574–24582 (2019).
70. Beaudoin, J.-D. et al. Analyses of mRNA structure dynamics identify embryonic gene regulatory programs. *Nat. Struct. Mol. Biol.* **25**, 677–686 (2018).
71. Patalano, S., Mihailovich, M., Belacortu, Y., Paricio, N. & Gebauer, F. Dual sex-specific functions of *Drosophila* Upstream of N-ras in the control of X chromosome dosage compensation. *Development* **136**, 689–698 (2009).
72. Elatmani, H. et al. The RNA-binding protein Unr prevents mouse embryonic stem cells differentiation toward the primitive endoderm lineage. *Stem Cells* **29**, 1504–1516 (2011).
73. Mitchell, S. A., Brown, E. C., Coldwell, M. J., Jackson, R. J. & Willis, A. E. Protein factor requirements of the Apaf-1 internal ribosome entry segment: roles of polypyrimidine tract binding protein and upstream of N-ras. *Mol. Cell. Biol.* **21**, 3364–3374 (2001).
74. Schepens, B. et al. A role for hnRNP C1/C2 and Unr in internal initiation of translation during mitosis. *EMBO J.* **26**, 158–169 (2007).
75. Guo, A.-X., Cui, J.-J., Wang, L.-Y. & Yin, J.-Y. The role of CSDE1 in translational reprogramming and human diseases. *Cell Commun. Signal.* **18**, 14 (2020).
76. Moore, K. S. et al. Csde1 binds transcripts involved in protein homeostasis and controls their expression in an erythroid cell line. *Sci. Rep.* **8**, 2628 (2018).
77. Wurth, L. et al. UNR/CSDE1 drives a post-transcriptional program to promote melanoma invasion and metastasis. *Cancer Cell* **30**, 694–707 (2016).
78. Horos, R. et al. Ribosomal deficiencies in Diamond-Blackfan anemia impair translation of transcripts essential for differentiation of murine and human erythroblasts. *Blood* **119**, 262–272 (2012).
79. Guo, H. et al. Disruptive variants of CSDE1 associate with autism and interfere with neuronal development and synaptic transmission. *Sci. Adv.* **5**, eaax2166 (2019).

80. Saltel, F. et al. Unr defines a novel class of nucleoplasmic reticulum involved in mRNA translation. *J. Cell Sci.* **130**, 1796–1808 (2017).
81. Sanders, S. J. et al. De novo mutations revealed by whole-exome sequencing are strongly associated with autism. *Nature* **485**, 237–241 (2012).
82. Kladwang, W., VanLang, C. C., Cordero, P. & Das, R. A two-dimensional mutate-and-map strategy for non-coding RNA structure. *Nat. Chem.* **3**, 954–962 (2011).
83. Cordero, P. & Das, R. Rich RNA structure landscapes revealed by mutate-and-map analysis. *PLoS Comput. Biol.* **11**, e1004473 (2015).
84. Bhaskaran, H. & Russell, R. Kinetic redistribution of native and misfolded RNAs by a DEAD-box chaperone. *Nature* **449**, 1014–1018 (2007).

Methods

Data sources. See Supplementary Notes for the publicly available data used in this study.

h5UTR definition. Sixty-way vertebrate PhastCons elements were downloaded from the UCSC mouse genome database, and elements with LOD ≥ 500 were subsetted. For each mouse RefSeq transcript record, the total number of 5′ UTR, CDS and 3′ UTR nucleotides overlapping LOD ≥ 500 elements were calculated (Supplementary Table 1). The 5′ UTRs with ≥250 nucleotide overlap were labeled hyperconserved. See Supplementary Notes for the full description.

Transcriptome–proteome correlations. Cross-tissue tandem mass tag mass spectrometry data and matching RNA-seq data were obtained from GTEx quantitative proteomics analysis of 32 human tissues from 14 individuals[27]. Pearson's correlation coefficient was calculated between per-tissue medians of RNA expression and per-tissue medians of protein expression. See Supplementary Notes for the full description of data-processing steps.

Term enrichment analysis. GO term enrichment analysis was performed using topGO (v.2.38.1)[85]. GO-term gene mappings were obtained from the Bioconductor annotation package org.Mm.eg.db. Mammalian phenotype ontology term enrichment analysis was performed using MouseMine[86]. See Supplementary Notes for the full description.

CRISPR knockouts. sgRNAs were designed using CRISPOR[87]. The sgRNA sequences were synthesized as single-stranded (ss) DNA oligonucleotides and were cloned into the BbsI-digested expression plasmid bearing both sgRNA scaffold backbone and Cas9 nuclease, pX330-U6-Chimeric_BB-CBh-hSpCas9. For HCE knockouts in mESCs (*Chrdl1*, *Dlx1*, *Sema3a* and *Zfx*), ~0.5×10^6 cells were plated onto a single 6-well plate (see Supplementary Table 9 for sgRNA sequences and genotyping primers). After 4 hours, 1.25 µg of each of the plasmids carrying sgRNA pairs were transfected using 2.5 µl of P3000 reagent and 12 µl of Lipofectamine 3000 (ThermoFisher Scientific, catalog no. L3000001). At 12 hours after transfection, the medium was changed to puromycin (ThermoFisher Scientific, catalog no. A1113803) containing media at 1 µg ml^{-1}. After 24 hours of puromycin selection, cells were washed with PBS, trypsinized and plated at 1,000 cells per 10-cm plate. Ten days later, single colonies were picked and replica plated to two 96-well plates. One plate was used for genotyping. For HCE knockout in 3T3 cells (*Gdf5*), the transfection and selection were performed using the same methods, but the cells were plated at limiting dilution of 0.5 cells per well into a 96-well plate for expansion and split for genotyping. Cells in the genotyping plate were lysed by removing the media, adding 100 µl of 50 mM NaOH per well and heating at 95 °C for 10 min. After cooling to room temperature, 500 µl of 500 mM Tris–HCl pH 8.0 was added to neutralize and a 1:100 dilution was taken for genotyping PCR. The genotyping PCR reaction was as follows: 1× MyTaq HS Red Mix (Meridian Biosceince, catalog no. BIO-25047), 300 nM forward primer, 300 nM reverse primer, 1 µl of 1:100 diluted crude lysate in 10 µl total reaction volume. Cycling conditions were: 95 °C, 3 min initial denaturation, followed by 30 cycles of 95 °C for 15 s, 68 °C for 15 s, 72 °C for 30 s. Clones with expected shorter amplicons were further expanded. DNA from expanded clones was isolated with Wizard Genomic DNA Purification kit (Promega, catalog np. A1120). The genotyping PCR reaction from expanded clones was as follows: 0.02 U µl^{-1} Kapa HiFi HotStart polymerase (Roche, catalog no. KR0369), 1× Kapa HiFi HotStart buffer, 300 µM dNTP each, 300 nM forward primer, 300 nM reverse primer, 10 ng genomic DNA in 20 µl. Cycling conditions were: 95 °C for 3 min initial denaturation, followed by 30 cycles of 98 °C for 20 s, 68 °C for 15 s, 72 °C for 30 s. The amplicons were Sanger sequenced at Quintara Biosciences.

Cell culture. See Supplementary Notes for the description of cell culture conditions.

Mouse husbandry. All animal work was reviewed and approved by the Stanford Administrative Panel on Laboratory Animal Care (APLAC). The Stanford APLAC is accredited by the American Association for the Accreditation of Laboratory Animal Care. All mice used in the study were housed at the Research Animal Facility) and at the SIM-1 Barrier Facility at Stanford University. All mice used for experiments were between two and six months old. All animal studies were performed in accordance with Stanford University Animal Care and Use guidelines.

Polysome profiling. Cells were collected 2 min after replacing media with cycloheximide (MilliporeSigma, catalog no. C7698-1G) containing media at 100 µg ml^{-1}. Approximately 10×10^6 cells were resuspended in 400 µl of the following lysis buffer on ice for 30 min, vortexing every 10 min: 25 mM Tris–HCl pH 7.5, 150 mM NaCl, 15 mM $MgCl_2$, 1 mM DTT, 8% glycerol, 1% Triton X-100, 100 µg ml^{-1} cycloheximide, 0.2 U µl^{-1} Superase-In RNase inhibitor (ThermoFisher Scientific, catalog no. AM2694), 1× Halt protease inhibitor cocktail (ThermoFisher Scientific, catalog no. 78430), 0.02 U µl^{-1} TURBO DNase (ThermoFisher Scientific, catalog no. AM2238). Nuclei were removed by two-step centrifuging, first at 1,300*g* for 5 min and then at 10,000*g* for 5 min, taking the supernatants from each. A 25%–50% sucrose gradient was prepared in 13.2-ml ultracentrifuge tubes (Beckman Coulter, catalog no. 331372) using Biocomp Gradient Master with the following recipe: 25 or 50% sucrose (w/v), 25 mM Tris–HCl pH 7.5, 150 mM NaCl, 15 mM $MgCl_2$, 1 mM DTT, 100 µg ml^{-1} cycloheximide. The lysate was layered onto the sucrose gradient and ultracentrifuged on a Beckman Coulter SW-41Ti rotor at 40,000 r.p.m. for 150 min at 4 °C. The gradient was density fractionated using Brandel BR-188 into 16× 750-µl fractions. In vitro transcribed spike-in luciferase RNA (50 pg) was added to each fraction. A 700-µl portion of each fraction was mixed with 100 µl of 10% SDS, 200 µl of 1.5 M sodium acetate and 900 µl of acid phenol–chloroform pH 4.5 (ThermoFisher Scientific, catalog no. AM9720), heated at 65 °C for 5 min and centrifuged at 20,000*g* for 15 min at 4 °C for phase separation. A 600-µl aqueous phase was mixed with 600 µl of 100% ethanol and RNA was purified on silica columns (Zymo, catalog no. R1013). For each fraction, up to 5 µg of RNA was DNase treated at 37 °C for 30 min using 0.2 U µl^{-1} TURBO DNase with 1 U µl^{-1} Superase-In in 30 µl and purified again on a silica column. RNA (100 ng) was reverse transcribed using iScript reverse transcriptase (Bio-Rad, catalog no. 1708890) in 10-µl reactions. qPCR was performed using SsoAdvanced Universal SYBR Green Supermix (Bio-Rad, catalog no. 1725270) with 2 µl of 1:4 diluted reverse transcription reaction and primer pairs targeting the HCE knockout h5UTR genes or the spike-in (see Supplementary Table 9 for primer sequences).

Ct values were normalized to Ct values of spike-in luciferase and plotted as proportions across the 16 fractions. The *t*-statistic and *P* value were calculated for difference in means between the two genotypes for each fraction. Each replicate comprises an independent culture (per genotype), sucrose gradient fractionation and qPCR quantification. Fisher combined *P* value was calculated for no difference across all fractions.

Reporter constructs for luciferase assays. Bicistronic reporter gateway plasmid, pRF_gwy, was constructed from pRF vector, which has an SV40 promoter and two reporter genes, *Renilla* luciferase and firefly luciferase, with multiple cloning sites in between them[88]. Gateway cassette A (ThermoFisher Scientific, catalog no. 11828029) was inserted in between *Renilla* and firefly luciferases, replacing the cloning sites using two EcoRI sites.

RNA normalizing reporter gateway plasmid, pRF_D1, was constructed from pRF vector by replacing the cloning sites with HCV IRES and inserting gateway cassette A in between AvrII and EcoRV sites upstream of *Renilla* luciferase. Downstream of the *Renilla* luciferase was the firefly luciferase and the HCV IRES between them, such that the HCV IRES-translated downstream firefly luciferase normalizes for differences in RNA levels to enable measurement of translation efficiency.

Full-length h5UTRs were synthesized and cloned into pENTR1A (ThermoFisher Scientific, catalog no. A10462) by SGI (sequences in Supplementary Table 1). Truncation variants were either synthesized or cloned by PCR from synthesized full-length sequences into pENTR1A vectors. Gateway LR Clonase II (ThermoFisher Scientific, catalog no. 11791020) was used to recombine the full-length or truncation variants into either pRF_gwy or pRF_D1 vectors.

Mutant *Csde1* 5′ UTRs were cloned by Gibson assembly reaction (NEB, catalog no. E2621S) using mutation-containing ssDNA templates with homology arms and two upstream/downstream fragments (sequences in Supplementary Table 9). Full-length wild-type and mutant *Csde1* 5′ UTRs were inserted ibn pGL3 (Promega, catalog no. E1751) plasmid in between EcoRI and NcoI sites upstream of firefly luciferase gene. The in vitro transcription template was amplified with T7 promoter sequence containing primer and in vitro transcribed using T7 RNA polymerase (NEB, catalog no. E2040S). The in vitro transcription RNAs were capped using Vaccinia virus capping enzyme (Cellscript, catalog no. C-SCCE0625) and polyA tailed using polyA polymerase (Cellscript, catalog no. C-PAP5104H).

Reporter transfection for luciferase assays. For DNA transfections, 200 ng of plasmid DNA was transfected to cells plated on 96-well plates. For 10T1/2 cells, mESCs, NSCs, limb mesenchyme culture and embryoid bodies, 0.5 µl of Lipofectamine 2000 (ThermoFisher Scientific, catalog no. 11668030) was used per one well. For neurons, 0.2 µl of Viafect (Promega, catalog no. E4981) was used per well. Cells were incubated for 4 h with transfection reagent, DNA in OptiMEM media (ThermoFisher Scientific, catalog no. 31985062). Cells were then washed with PBS, and the medium was changed back to regular growth media.

For RNA transfection, 200 ng of firefly luciferase RNA and 10 ng of *Renilla* luciferase RNA was transfected to cells plated on 96-well plates. Lipofectamine 2000 (0.5 µl) was used per one well.

Luciferase assays. For DNA transfections, cells were lysed using Passive Lysis Buffer (Promega, catalog no. E1941) for 30 min at room temperature, 48 hours after transfection. For RNA transfections, cells were lysed 6 hours after transfection. Firefly and *Renilla* luciferase values were read using Dual-Glo Luciferase Assay System (Promega, catalog no. E2920) for >96 samples or Dual-Luciferase Reporter Assay System (Promega, catalog no. E1910) for fewer samples, on a Promega GloMax-Multi plate reader. In all experiments, log ratios of the two luciferase activities were taken for each well.

For bicistronic reporter assays across multiple cell types, the data were quantile normalized across all replicate samples. The normalmixEM function from R package mixtools (v.1.2.0) was used for mixture modeling of maximum replicate-average values. False discovery estimate at a cut-off was calculated as the proportion of the mixture distribution above the chosen cut-off that comes from the lower component. For identification of h5UTRs with significant differential activity across cell types, the *F*-statistic was calculated, and the Benjamini–Hochberg procedure used with their *P* values to estimate the FDR. Each replicate consisted of an independent reporter transfection, lysate collection and luciferase activity quantification.The luciferase activity data across cell types were clustered using pairwise Euclidean distance metric between h5UTRs and average linkage hierarchical clustering. For other reporter assays, all statistics were calculated from log ratios of the luciferase activities (two-sided *t*-test, Welch). Each replicate consisted of an independent reporter transfection, lysate collection and luciferase activity quantification. Mean and error bars when plotted in linear scale were back-transformed from the mean and standard errors of the log-scale values.

In-cell DMS probing following ATP depletion and multiplexed mutational profiling. One hundred h5UTRs were chosen for amplicon sequencing on the basis of coverage profiles from ENCODE E14 mESC RNA-seq data. See Supplementary Notes for the description of amplicon sequencing primer design and pooling. For ATP depletion, 10×10^6 mESCs were incubated for 10 min in ATP depletion media: DMEM without glucose (ThermoFisher Scientific, catalog no. A1443001), 10 mM 2-deoxy-D-glucose (2DG, MilliporeSigma, catalog no. 25972), 10 mM sodium azide (MilliporeSigma, catalog no. 71289). The cells were washed, trypsinized and collected using PBS, trypsin and finally resuspended in 3.5 ml of mESC media all containing 10 mM 2DG and 10 mM NaN_3. Bicine (1 ml, 1 M; MilliporeSigma, catalog no. B3876) titrated to pH 8.5 at 25 °C was added to resuspended cells (200 mM final bicine concentration). A portion of 500 µl of 16% dimethyl sulfate (MilliporeSigma, catalog no. D186309) in ethanol was added (1.6% final concentration). Cells were mixed and incubated for 6 min at 37 °C. Ice-cold 30% BME (2.5 ml; MilliporeSigma, catalog no. M3148) in ethanol was added to quench the reaction. This DMS modification protocol was adapted from protocol and data reported in ref. [69]). Following centrifugation to remove the supernatant, the cells were lysed in Trizol (ThermoFisher Scientific, catalog no. 15596026). For the untreated condition without ATP depletion treatment, all procedures were the same except for an initial 10-min incubation in ATP depletion media and inclusion of 2DG and NaN_3 in all media. Three independent samples were collected for each condition. Total RNA was phase extracted with chloroform and the aqueous phase was purified on silica columns (Zymo, catalog no. R1013). RNA (10–20 µg) was DNase treated at 37 °C for 30 min using 0.2 U µl^{-1} TURBO DNase (ThermoFisher Scientific, catalog no. AM2238) with 1 U µl^{-1} Superase-In (ThermoFisher Scientific, catalog no. AM2696) in 60 µl and purified again on a silica column.

RNA (1 µg) was mixed with 1 µl of 1 µM 96× primer pool (96×1 µM amplicon reverse primers for total of 1 µM oligonucleotides) and denatured in 6.25 µl total volume (with H_2O) at 65 °C for 2 min, then chilled to 4 °C. Reverse transcription reaction conditions were as follows: 20 mM Tris–HCl pH 7.5, 75 mM KCl, 10 mM $MgCl_2$, 5 mM DTT, 500 nM TGIRT (InGex, catalog no. TGIRT50), 1 U µl^{-1} Superase-In; 9 µl total reaction volume. The reverse transcription (RT) reaction was preincubated at 25 °C for 30 min, then initiated with addition of 1 µl of 12.5 mM dNTP each. After incubation at 60 °C for 1 hour, 1 µl of 2.5 M NaOH was added and the reaction heated at 95 °C for 3 min. Then 1 µl of 2.5 M HCl and 1 µl of 500 mM Tris–HCl pH 7.5 were added to neutralize. SPRIselect beads (29 µl; Beckman Coulter, catalog no. B23318) were used for purification of cDNA; the elution volume was 6 µl. Pooled reactions (4×96) for a total of 384 targets were performed for each sample. To each set of 96 pooled cDNA, multiplex PCR was performed with 5 µl of cDNA, 0.2 mM dNTP, 2 µM 96× forward primer pool (96× 2 µM each primer for a total of 2 µM oligonucleotides), 2 µM reverse primer pool, 1× SYBR Green I (ThermoFisher Scientific, catalog no. S7563), 0.02 U µl^{-1} Q5 HotStart DNA polymerase (NEB, catalog no. M0493S), 1× Q5 HotStart Reaction Buffer, 1× Q5 HotStart High GC Enhancer, in a total reaction volume of 30 µl. Cycling conditions were: 98 °C for 30 s initial denaturation, followed by 15–25 cycles (terminated before plateau) of 98 °C for 10 s, 56 °C for 40 s, 76 °C for 10 s. PCR was run for 15–25 cycles. Each 96-pool multiplex PCR reaction was then used in a master mix of second PCR with 96 individual primer pair reactions: 0.2 mM dNTP, 500 nM forward primer, 500 nM reverse primer, 1× SYBR Green I, Q5 HotStart DNA polymerase, 1× Q5 HotStart Reaction Buffer, 1× Q5 HotStart High GC Enhancer, in a total reaction volume of 6 µl. Cycling conditions were: 98 °C for 30 s initial denaturation, followed by 20 cycles of 98 °C for 10 s, 62 °C for 10 s, 76 °C for 10 s. The 384 individual reactions were pooled and purified on silica columns (NEB, catalog no. T1030S). The amplicon pool was end-prepared, Illumina adapter sequences were ligated, adapter-ligated DNA was size selected with SPRIselect beads for 370 bp and three-cycle barcoding PCR was performed (NEB, catalog no. E7645S). The 2× 150-bp paired-end sequencing data were generated on an Illumina HiSeq 4000 at Novogene.

One-dimensional accessibility data analysis. Briefly, per-nucleotide statistical significance of differential mutation rates were calculated using the voom-limma (v.3.42.2) method from the TMM-normalized mutation count matrix[89–91]. For per-window accessibility pattern differences, we calculated the Anderson–Darling statistic in sliding 11-nucleotide windows between per-nucleotide *t*-statistic values of the window versus the whole amplicon. False discovery rates were estimated by the Benjamini–Hochberg procedure. See Supplementary Notes for the full description.

In-cell mutate-and-map. Error-prone PCR was performed as follows: 0.05 U µl^{-1} of Mutazyme II (Agilent, catalog no. 200550), 1× Mutazyme II buffer, 1× SYBR, 200 µM dNTP each, 300 nM forward primer, 300 nM reverse primer, 100 pg *Csde1* 5′ UTR fragment; 95 °C for 2 min initial denaturation, 10 cycles of 95 °C for 30 s, 63 °C for 20 s, 72 °C for 1 min. See Supplementary Table 9 for the primers. A 100-pg input amount was determined by initially varying the input amounts to determine the amount at which the PCR was in exponential phase (50% of signal plateau). These parameters result in a mutation rate of approximately 1 per 200 nucleotides (Supplementary Fig. 7). The error-prone PCR amplicon has homology arms for Gibson assembly into pcDNA5/FRT (ThermoFisher Scientific, catalog no. V601020) plasmid with EGFP. The final construct has a flanking primer region for cDNA amplification upstream of the mutagenized 5′ UTR and EGFP open reading frame downstream. NEB 10-beta *Escherichia coli* cells (NEB, catalog no. C3020K) were transformed by electroporation and plated over a total of 2,000 cm^2 to give ~10,000 colonies. The plate was scraped and the mutagenesis library plasmid pool was purified.

mESCs were grown, dissociated and resuspended at 5×10^5 cells per ml. Mutagenesis library plasmid pool DNA (3 µg) and 7.5 µl of Lipofectamine 2000 in 100 µl of OptiMEM (ThermoFisher Scientific, catalog no. 31985062) were mixed with 2 ml of cells (1×10^6 cells) in mESC media. The cells were incubated for 10 min in suspension, centrifuged, washed with mESC media and plated into one well in a 6-well plate. At 24 hours after transfection, the cells were washed, trypsinized and resuspended in 3.5 ml of mESC media. Bicine (1 ml, 1 M; MilliporeSigma, catalog no. B3876), titrated to pH 8.5 at 25 °C, was added to resuspended cells (200 mM final bicine concentration). A total of 500 µl of 16% dimethyl sulfate (MilliporeSigma, catalog no. D186309) in ethanol was added (1.6% final concentration). Cells were mixed and incubated for 6 min at 37 °C. Ice-cold 30% BME (2.5 ml; MilliporeSigma, catalog no. M3148) in ethanol was added to quench the reaction. Following centrifugation to remove the supernatant, the cells were lysed in Trizol (ThermoFisher Scientific, catalog no. 15596026). Total RNA was phase extracted with chloroform and the aqueous phase purified on silica columns (Zymo, catalog no. R1013). RNA (10–20 µg) was DNase treated at 37 °C for 30 min using 0.2 U µl^{-1} TURBO DNase (ThermoFisher Scientific, catalog no. AM2238) with 1 U µl^{-1} Superase-In (ThermoFisher Scientific, catalog no. AM2696) in 60 µl and purified again on a silica column. For in vitro probing, IVT template was first amplified from the mutagenesis library plasmid pool by using a T7 promoter sequence containing primer and transcribed with T7 RNA polymerase (NEB, catalog no. E2040S). The IVT RNAs were capped with Vaccinia virus capping enzyme (Cellscript, catalog no. C-SCCE0625) and polyA tailed with polyA polymerase (Cellscript, catalog no. C-PAP5104H). Then 200 ng IVT RNA was denatured for 2 min at 95 °C and brought to 37 °C. IVT RNA was then folded for 30 min in the following solution conditions: 200 mM bicine, pH 8.5, 100 mM NaCl 5.5 mM $MgCl_2$, 10 µl total volume. Subsequently, 1 µl 16% dimethyl sulfate (MilliporeSigma, catalog no. D186309) in ethanol was added (1.6% final concentration) and incubated for 6 min at 37 °C. Finally, 4 µl BME (MilliporeSigma, catalog no. M3148) was added to quench the reaction, and RNA was purified on silica columns (Zymo, catalog no. R1013).

RNA (1 µg) was mixed with 1 µl of 1 µM RT primer targeting the downstream EGFP and denatured in 6.25 µl total volume (with H_2O) at 65 °C for 2 min, then chilled to 4 °C. Reverse transcription reaction conditions were as follows: 20 mM Tris–HCl pH 7.5, 75 mM KCl, 10 mM $MgCl_2$, 5 mM DTT, 500 nM TGIRT (InGex, catalog no. TGIRT50), 1 U µl^{-1} Superase-In, 9 µl total reaction volume. The RT reaction was preincubated for 25 °C for 30 min, then initiated with addition of 1 µl of 12.5 mM dNTP each. After incubation at 60 °C for 1 hour, 1 µl of 2.5 M NaOH was added and the reaction heated at 95 °C for 3 min. Then 1 µl of 2.5 M HCl and 1 µl of 500 mM Tris–HCl pH 7.5 was added to neutralize. SPRIselect beads (29 µl; Beckman Coulter, B23318) were used for purification of cDNA; elution volume was 7 µl. PCR reaction was performed as follows: 0.2 mM dNTP, 300 nM forward primer, 300 nM reverse primer, 1× SYBR Green I (ThermoFisher Scientific, catalog no. S7563), 0.02 U µl^{-1} Q5 HotStart DNA polymerase (NEB, catalog no. M0493S), 1× Q5 HotStart Reaction Buffer, 1× Q5 HotStart High GC Enhancer, 2 µl of cDNA, in a total reaction volume of 20 µl. Cycling conditions were: 98 °C for 30 s initial denaturation, 20 cycles of 98 °C for 10 s, 64 °C for 10 s, 72 °C for 30 s; 20 cycles with full-length amplicon primers. The reaction was diluted 100-fold and used as a template in the second round of PCR with the same conditions but using primers for 3×250 nucleotide shorter tiling amplicons for 10 cycles. See Supplementary Table 9 for the RT and PCR primers. The reactions were purified on silica columns and pooled. The pooled DNA was end-prepared, Illumina adapter sequences were ligated, adapter-ligated DNA was size selected with SPRIselect beads for 370 bp and three-cycle barcoding PCR was performed (NEB, catalog no. E7645S). The 2× 150-bp paired-end sequencing data were generated on an Illumina HiSeq 4000 at Novogene.

Two-dimensional accessibility data analysis and structure models. Briefly, the normalized covariation matrix was clustered using multidimensional scaling, $K=2$. Cluster average accessibility z-scores were used to constrain partition function calculation in Vienna RNA (v.2.4.14)[92]. A total of 250 structures were sampled for each cluster and used as input suboptimals to REEFFIT (v.0.6.3)[83]. For visualization of the landscape, we used pairwise distance metrics, structure clustering and medoid assignment produced by REEFFIT, and sum of weights for structures belonging to each of the three clusters represented by a medoid structure are presented in the main figure. Bootstrapping was used to estimate population fraction errors. See Supplementary Notes for the full description.

Reporting Summary. Further information on research design is available in the Nature Research Reporting Summary linked to this article.

Data availability

Raw sequencing data (related to Figs. 4, 5 and 6) are deposited to GEO with accession code GSE155656. Processed reactivity data have been deposited in the RNA Mapping Database (RMDB) with accession codes CSDE1_DMS_0000 and CSDE1_DMS_0001. Sources for publicly available data are described in the Methods.

Code availability

All software used to analyze the study data are listed in the Methods and in the Nature Research Reporting Summary and are publicly available. All codes used to analyze icM^2 data are available through a Github repository: github.com/barnalab/icm2p.

References

85. Alexa, A., Rahnenführer, J. & Lengauer, T. Improved scoring of functional groups from gene expression data by decorrelating GO graph structure. *Bioinformatics* **22**, 1600–1607 (2006).
86. Motenko, H., Neuhauser, S. B., O'Keefe, M. & Richardson, J. E. MouseMine: a new data warehouse for MGI. *Mamm. Genome* **26**, 325–330 (2015).
87. Concordet, J.-P. & Haeussler, M. CRISPOR: intuitive guide selection for CRISPR/Cas9 genome editing experiments and screens. *Nucleic Acids Res.* **46**, W242–W245 (2018).
88. Yoon, A. et al. Impaired control of IRES-mediated translation in X-linked dyskeratosis congenita. *Science* **312**, 902–906 (2006).
89. Robinson, M. D. & Oshlack, A. A scaling normalization method for differential expression analysis of RNA-seq data. *Genome Biol.* **11**, R25 (2010).
90. Law, C. W., Chen, Y., Shi, W. & Smyth, G. K. voom: precision weights unlock linear model analysis tools for RNA-seq read counts. *Genome Biol.* **15**, R29 (2014).
91. Ritchie, M. E. et al. limma powers differential expression analyses for RNA-sequencing and microarray studies. *Nucleic Acids Res.* **43**, e47 (2015).
92. Lorenz, R. et al. ViennaRNA Package 2.0. *Algorithms Mol. Biol.* **6**, 26 (2011).

Acknowledgements

We thank the members of the Barna laboratory for constructive criticism of the manuscript. This work was supported by New York Stem Cell Foundation grant NYSCF-R-I36 (M.B.), NIH grant 1R01HD086634 (M.B.), Alfred P. Sloan Research Fellowship (M.B.), Pew Scholars Award (M.B.), Mallinckrodt Foundation Award (M.B.), Benchmark Stanford Graduate Fellowship (G.W.B.) and Walter and Idun Berry Foundation (E.S.C.). M.B. is a New York Stem Cell Robertson Investigator.

Author contributions

M.B., G.W.B. and E.S.C. conceived the project. M.B. supervised the project. L.J. and H.T. provided the GTEx data and critical feedback on its analysis. R.D. provided critical feedback on the development and analysis of icM^2. E.S.C. carried out the large-scale reporter screens. G.W.B. performed all other experiments and data analysis. G.W.B. and M.B. wrote the manuscript in consultation with all authors.

Competing interests

The authors declare no competing interests.

Additional information

Extended data is available for this paper at https://doi.org/10.1038/s41588-021-00830-1.

Supplementary information The online version contains supplementary material available at https://doi.org/10.1038/s41588-021-00830-1.

Correspondence and requests for materials should be addressed to M.B.

Peer review information *Nature Genetics* thanks Jean-Denis Beaudoin, Philip Bevilacqua and the other, anonymous, reviewer(s) for their contribution to the peer review of this work. Peer reviewer reports are available.

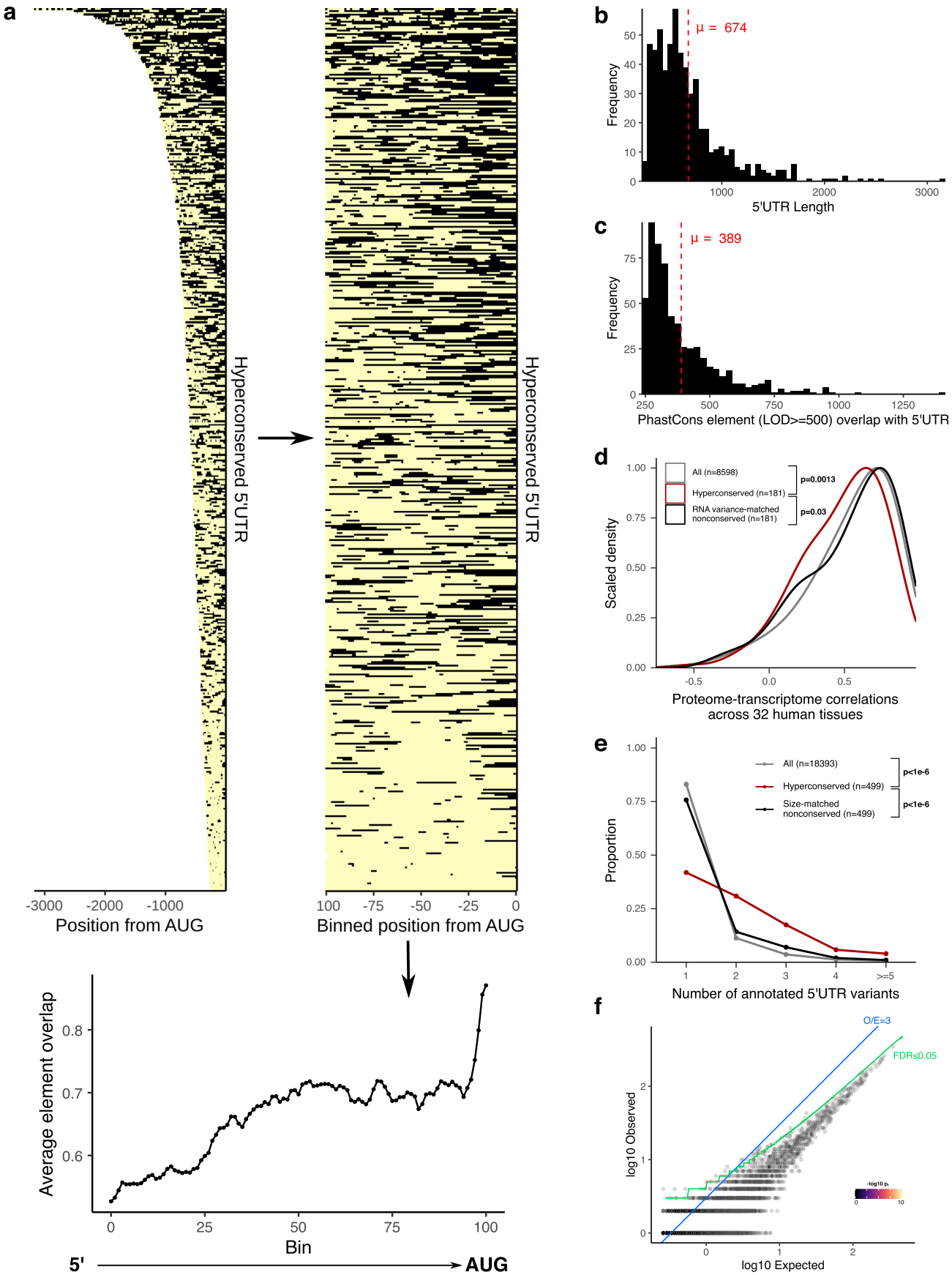

Extended Data Fig. 1 | See next page for caption.

Extended Data Fig. 1 | Hyperconserved 5′UTRs in vertebrate genomes. a, Left: heatmap of the positions of LOD ≥ 500 PhastCons elements in each h5UTR. Middle: heatmap of the relative positions (calculated in 100 bins across the h5UTRs) of the elements. Right: plot of average element overlap across the 100 bins to illustrate the positional preference. **b**, Histogram of the length of h5UTRs. Average length is 674nt. **c**, Histogram of the number of nucleotides overlap between LOD ≥ 500 PhastCons elements and h5UTRs. Average overlap is 389nt. **d**, Distributions of cross-tissue transcriptome-proteome correlations for all genes, genes with h5UTRs, or genes with variance-matched non-conserved 5′UTRs. Indicated p-values are from two-sided Wilcoxon rank sum tests for cross-tissue correlation values between h5UTR genes and all genes or between h5UTR genes and variance-matched non-conserved controls. **e**, Distributions of the number of annotated alternative 5′UTRs for all genes, genes with h5UTRs, or genes with size-matched non-conserved 5′UTRs. Indicated p-values are from two-sided Wilcoxon rank sum tests for the number of alternative 5′UTRs between h5UTR genes and all genes or between h5UTR genes and size-matched non-conserved controls. **f**, Scatter plot illustrating the lack of significant term enrichments for a size-matched set of non-conserved 5′ UTRs. X-axis and y-axis plots expected and the observed number of genes for each term. Blue dashed line indicates the minimum observed/expected ratio cutoff of 3. Green line indicates expected and observed counts where Fisher's test p-value (p_f) is estimated to have FDR = 0.05. Neighbor-weighted test p-value (p_{fw}) ≤0.05 is further used as an additional cutoff. The final set of enriched terms passing filter is colored by p_f and sized by p_{fw}.

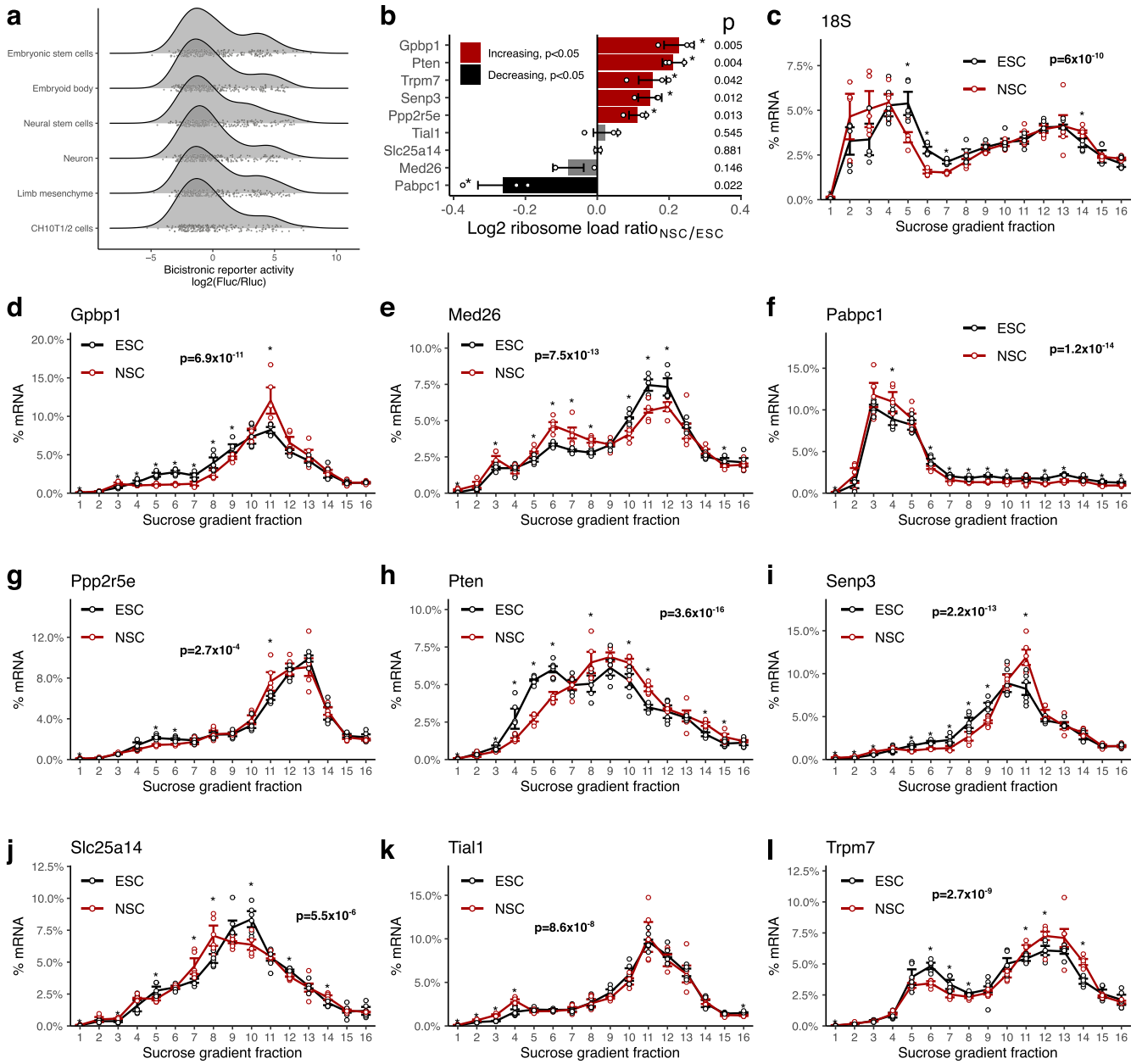

Extended Data Fig. 2 | Non-canonical translation activation by hyperconserved 5'UTRs across cell types. a, Density plots of non-canonical translation initiation activities from h5UTRs by bicistronic reporter assay. X-axis is the luciferase reporter activity ratios. Jittered dots mark individual reporter ratios for each h5UTR in each cell type. **b**, Summarized plot of ribosome load (sum of % mRNA times the ribosome number for each fraction) differential ratio between NSCs and ESCs calculated from polysome profiles for each gene shown in Extended Data Fig. 2c-l. Red indicates significant increase in NSCs and black indicates significant decrease (two-sided t-test $p \leq 0.05$, $n = 3$, marked by asterisk). **c-l**, Endogenous polysome profiles of NSCs versus ESCs for genes with h5UTRs that show high non-canonical translation reporter activities in NSCs compared to ESCs. Distribution of mRNAs across sucrose gradient fractions are plotted. Y-axis plots the mean percent mRNA. Error bars indicate standard error. Asterisk indicates two-sided t-test $p \leq 0.05$ for each fraction between the two cell types. $n = 3$ for each cell type. Indicated p-value (p_f) is calculated by Fisher's method across all fractions. Note that Extended Data Fig. 2c shows the profile of 18 S rRNA, which indicates lower global translation in NSCs compared to ESCs.

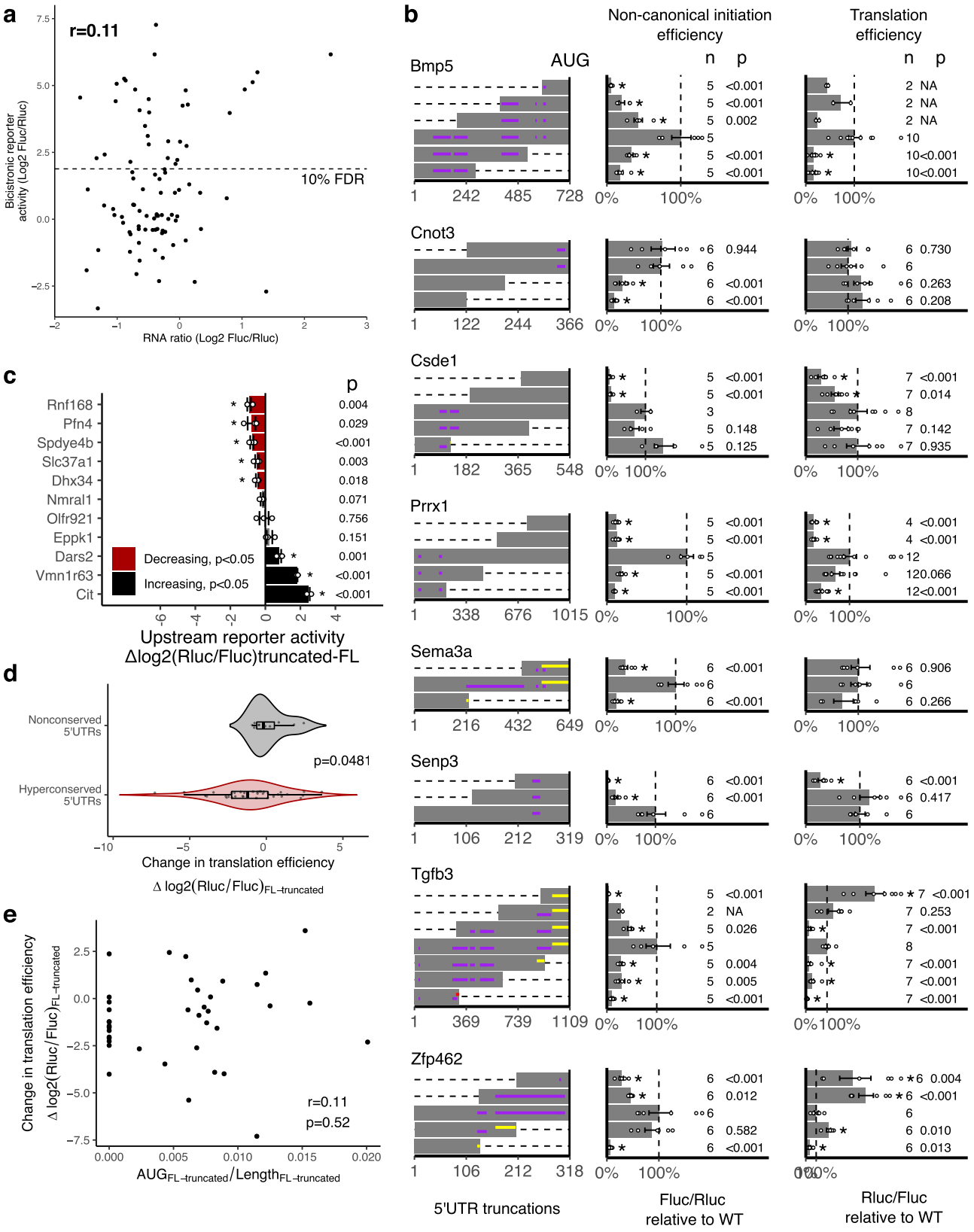

Extended Data Fig. 3 | See next page for caption.

Extended Data Fig. 3 | Non-canonical activation by hyperconserved 5′UTRs substantially contributes to translation. a, Scatter plot of luciferase activity versus RNA level ratios (mean from n = 3) observed for the bicistronic reporters of 90 h5UTRs measured in 10T1/2 cells. Dashed line marks the 10% FDR used in Fig. 3a. Spearman correlation indicated on top left. **b**, The effect of various truncations of the h5UTRs on non-canonical initiation and total translation efficiency (also see Fig. 3d). Left: positions of truncations. Dashed lines indicate truncations. Purple horizontal lines indicate uORFs; yellow and red lines indicate in-frame and out-of-frame uAUGs, respectively. Middle: non-canonical initiation efficiency. Right: total translation efficiency. X-axis indicates the mean of luciferase reporter ratios relative to the wild-type. Error bars indicate standard error. Dashed line marks the wild-type 5′UTR activity. Asterisk indicates two-sided t-test $p \leq 0.05$ for each truncation versus the full-length. The numbers to the left of the bars indicate n and p-values. **c**, Comparison of translational activities between the full-length long, non-conserved 5′UTRs versus the only first 300nt truncation. 11 different pairs are tested. X-axis indicates the mean log2 luciferase reporter ratios of each truncation relative to its full-length wild-type. Error bars indicate standard error. Bars colored in red indicate significantly reduced translation in the shorter, truncated 300nt fragment; black indicates significant increase (two-sided t-test, paired $n = 3$, $p \leq 0.05$, marked by asterisk). The numbers to the left of the bars indicate p-values. **d**, Violin plot of full-length/truncated reporter activity ratios (log2) from hyperconserved and non-conserved 5′UTRs. p indicates two-sided Wilcoxon rank sum test p-value. Box hinges: 25% quantile, median, 75% quantile, respectively from left to right. Whiskers: lower or upper hinge ±1.5*IQR. **e**, Scatter plot of change in translation efficiency between full-length and truncated h5UTRs shown in Fig. 3e versus change in uAUG density (change in number of AUGs / change in length between each pair of full-length and truncated h5UTRs). r indicates pearson's correlation coefficient and p indicates two-tailed p-value.

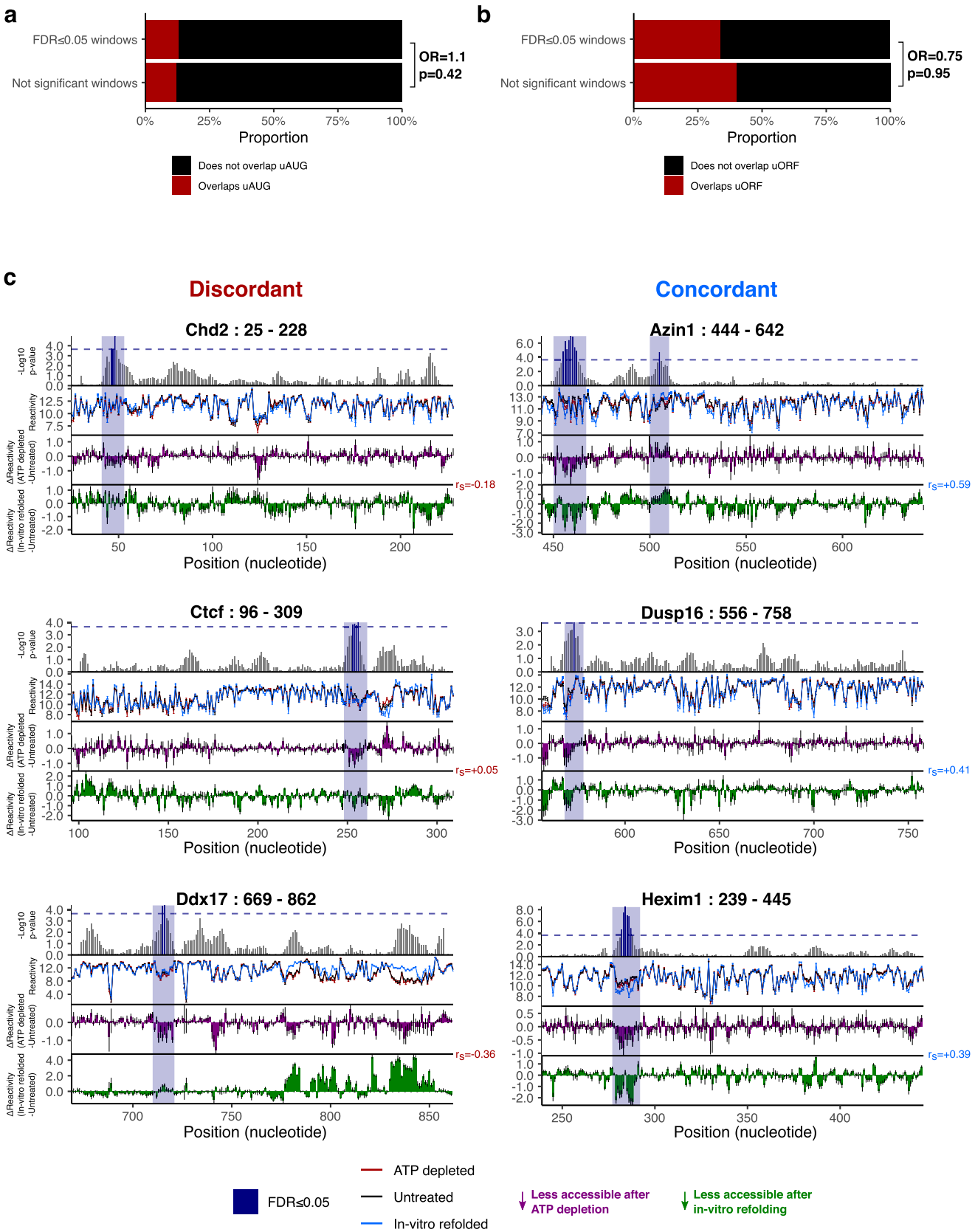

Extended Data Fig. 4 | See next page for caption.

Extended Data Fig. 4 | Cellular remodeling of hyperconserved 5′UTR RNA structures. a, Stacked bar plots showing proportions of significant (FDR ≤ 0.05) or not significant windows that overlap uAUG in black versus that do not overlap uAUG in red. OR indicates odds ratio for overlaps uAUG / does not overlap uAUG, and p indicates Fisher's test p-value (one-sided, H_a = odds ratio>0). **b**, Stacked bar plots showing proportions of significant (FDR ≤ 0.05) or not significant windows that overlap uORF in black versus that do not overlap uORF in red. OR indicates odds ratio for overlaps uORF / does not overlap uORF, and p indicates Fisher's test p-value (one-sided, H_a = odds ratio>0). **c**, Zoomed-in view of differential accessibilities along h5UTRs with one or more significantly different windows under ATP depletion. Top plot shows -log10 p-value for each window. Highlighted boxes mark significantly different windows, above the dashed line indicating 5% FDR. Middle plot shows differential accessibility on the y-axis, where greater than zero indicates increased accessibility upon ATP depletion and less than zero indicates decreased accessibility. Bottom plot shows differential accessibility for in vitro refolded RNA. Error bars in each plot show standard error, n = 3. The three profiled regions shown on the left side exhibit discordant profiles between accessibility changes observed in cells following ATP depletion and accessibility changes observed for in cell versus in vitro refolded RNA. The other three on the right side exhibit concordant profiles.

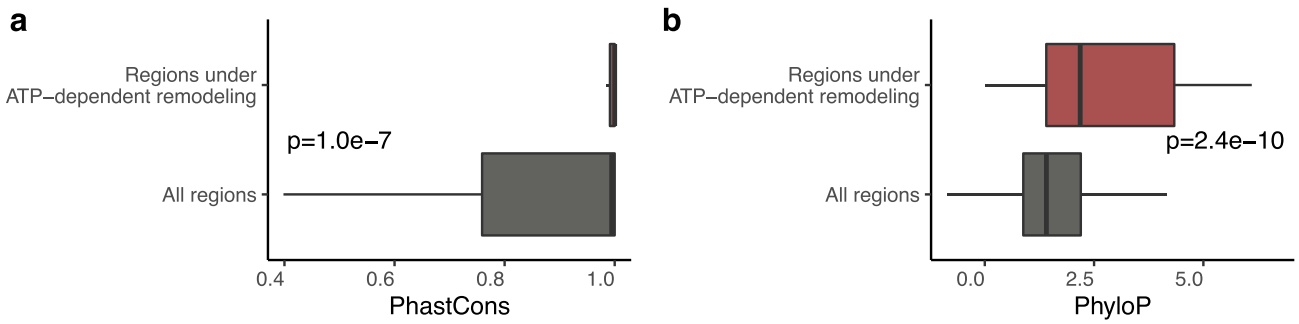

Extended Data Fig. 5 | icM² reveals structured elements in the hyperconserved Csde1 5′UTR. a, Boxplot of average PhastCons scores in significant windows of ATP-dependent remodeling versus all windows shown in Fig. 4c. p indicates two-sided Wilcoxon rank sum test p-value. **b**, Same as Extended Data Fig. 5a, but showing the distribution of average PhyloP scores.

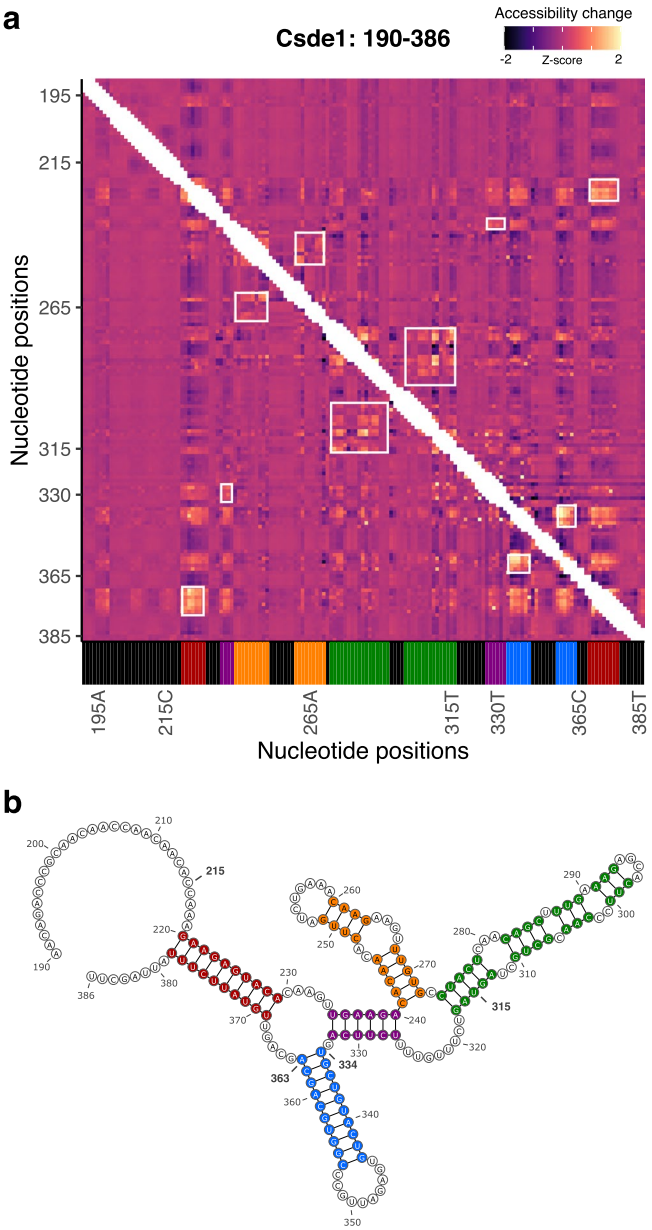

Extended Data Fig. 6 | In-vitro M² analysis of Csde1 5′UTR. a, Heatmap of in-vitro M² accessibility matrix for *Csde1* 5′UTR from position 190 to 386. For each row, the chemical mapping profile of a single-nucleotide variant of the RNA is plotted across the columns, where the colors indicate z-scaled accessibility change values from the wild-type RNA. 1D data from each mutant are vertically stacked to display a 2D matrix. White boxes mark perturbation signals that support the model shown in Extended Data Fig. 6b; color bars at the bottom indicate the nucleotide positions of the stems that match the same color in the model. **b**, The model for the in-vitro structure of *Csde1* 5′UTR from position 190 to 386. Also see Extended Data Fig. 6a.

nature research

Corresponding author(s): Maria Barna

Last updated by author(s): Jan 31, 2021

Reporting Summary

Nature Research wishes to improve the reproducibility of the work that we publish. This form provides structure for consistency and transparency in reporting. For further information on Nature Research policies, see our Editorial Policies and the Editorial Policy Checklist.

Statistics

For all statistical analyses, confirm that the following items are present in the figure legend, table legend, main text, or Methods section.

n/a	Confirmed
☐	☒ The exact sample size (*n*) for each experimental group/condition, given as a discrete number and unit of measurement
☐	☒ A statement on whether measurements were taken from distinct samples or whether the same sample was measured repeatedly
☐	☒ The statistical test(s) used AND whether they are one- or two-sided *Only common tests should be described solely by name; describe more complex techniques in the Methods section.*
☒	☐ A description of all covariates tested
☐	☒ A description of any assumptions or corrections, such as tests of normality and adjustment for multiple comparisons
☐	☒ A full description of the statistical parameters including central tendency (e.g. means) or other basic estimates (e.g. regression coefficient) AND variation (e.g. standard deviation) or associated estimates of uncertainty (e.g. confidence intervals)
☐	☒ For null hypothesis testing, the test statistic (e.g. *F*, *t*, *r*) with confidence intervals, effect sizes, degrees of freedom and *P* value noted *Give P values as exact values whenever suitable.*
☒	☐ For Bayesian analysis, information on the choice of priors and Markov chain Monte Carlo settings
☒	☐ For hierarchical and complex designs, identification of the appropriate level for tests and full reporting of outcomes
☐	☒ Estimates of effect sizes (e.g. Cohen's *d*, Pearson's *r*), indicating how they were calculated

Our web collection on statistics for biologists contains articles on many of the points above.

Software and code

Policy information about availability of computer code

Data collection	ThermoAlign 1.0.0; PrimerPooler 1.41; cutadapt 1.18; BBMerge 38.22; bowtie2 2.3.4.3; samtools 1.9; UMI-tools 0.5.4; shapemapper 2.1.5 Data processing using these softwares is detailed in Online Methods section, and the pipeline scripts are available on github.com/barnalab/icm2p
Data analysis	ViennaRNA 2.4.14; REEFFIT 0.6.3; R 3.6.2 with packages tidyverse 1.3.0, limma 3.42.2, edgeR 3.28.1, Biostrings 2.54.0, viridis 0.5.1, data.table 1.12.8, kSamples 1.2.9, ggrepel 0.8.2, impute 1.60.0, mixtools 1.2.0, topGO 2.38.1, ggridges 0.5.2, GOSemSim 2.12.1, zoo 1.8.7, igraph 1.2.5, cowplot 1.0.0 Analysis methods and parameters are described in Online Methods. The analysis codes used are available in full at github.com/barnalab/icm2p.

For manuscripts utilizing custom algorithms or software that are central to the research but not yet described in published literature, software must be made available to editors and reviewers. We strongly encourage code deposition in a community repository (e.g. GitHub). See the Nature Research guidelines for submitting code & software for further information.

Data

Policy information about availability of data

All manuscripts must include a data availability statement. This statement should provide the following information, where applicable:

- Accession codes, unique identifiers, or web links for publicly available datasets
- A list of figures that have associated raw data
- A description of any restrictions on data availability

Raw sequencing data (related to Figs. 4, 5 and 6) are deposited to GEO with accession code GSE155656. The following lists the version and sources of publicly available data used in this study. RefSeq: release 84, https://ftp.ncbi.nlm.nih.gov/refseq/; 60-way PhastCons: UCSC mm10, http://hgdownload.soe.ucsc.edu/

goldenPath/mm10/phastCons60way/, http://hgdownload.soe.ucsc.edu/goldenPath/mm10/database/; 60-way multiple sequence alignment: UCSC mm10, http://hgdownload.soe.ucsc.edu/goldenPath/mm10/multiz60way/; GTEX RNA-seq: V8 (GENCODE V25 annotation), https://www.gtexportal.org/home/datasets, ; GO term mapping: Bioconductor 3.10 org.Mm.eg.db, http://bioconductor.org/packages/3.10/data/annotation/html/org.Mm.eg.db.html; ENCODE: https://www.encodeproject.org/.

Field-specific reporting

Please select the one below that is the best fit for your research. If you are not sure, read the appropriate sections before making your selection.

☒ Life sciences ☐ Behavioural & social sciences ☐ Ecological, evolutionary & environmental sciences

For a reference copy of the document with all sections, see nature.com/documents/nr-reporting-summary-flat.pdf

Life sciences study design

All studies must disclose on these points even when the disclosure is negative.

Sample size	Samples analyzed were chosen based on the expected potential effect sizes and based on the variability typically seen for each types of experiments performed as previously observed in the literature or practically experienced by the field.
Data exclusions	Low coverage amplicons are excluded from analysis. While the quantitative criteria for exclusion were not pre-established prior to the study, dropouts in amplicon sequencing are both expected and obviously distinguished by analyzing its coverage and per-amplicon replicate correlations. Final quality control criteria for the amplicon sequencing data are empirically determined and detailed in the Online Methods section.
Replication	Each replicate comprises an independent cell culture, sample collection and quantitative analysis per genotype or condition. The exact number of replications vary for different experiments but are always clearly indicated in each figure panel or legend.
Randomization	Randomization is not relevant because genotypes or conditions were constructed and there was no subjective allocation of samples to experimental groups.
Blinding	Blinding was not considered in this study as the experiments are not based on subjective measurements.

Reporting for specific materials, systems and methods

We require information from authors about some types of materials, experimental systems and methods used in many studies. Here, indicate whether each material, system or method listed is relevant to your study. If you are not sure if a list item applies to your research, read the appropriate section before selecting a response.

Materials & experimental systems

n/a	Involved in the study
☒	☐ Antibodies
☐	☒ Eukaryotic cell lines
☒	☐ Palaeontology and archaeology
☐	☒ Animals and other organisms
☒	☐ Human research participants
☒	☐ Clinical data
☒	☐ Dual use research of concern

Methods

n/a	Involved in the study
☒	☐ ChIP-seq
☒	☐ Flow cytometry
☒	☐ MRI-based neuroimaging

Eukaryotic cell lines

Policy information about cell lines

Cell line source(s)	E14Tg2a.4; C3H/10T1/2, Clone 8 (ATCC CCL-226); NIH/3T3 (ATCC CRL-1658)
Authentication	Cell lines are not authenticated.
Mycoplasma contamination	Cell lines were not tested for mycoplasma.
Commonly misidentified lines (See ICLAC register)	No commonly misidentified cell lines were used in this study.

Animals and other organisms

Policy information about studies involving animals; ARRIVE guidelines recommended for reporting animal research

Laboratory animals	Species: Mus musculus; Strain: C57BL/6J; Sex: female; Age: 2-6 months
Wild animals	This study did not involve wild animals.
Field-collected samples	This study did not involve samples collected from the field.
Ethics oversight	All animal work was reviewed and approved by the Stanford Administrative Panel on Laboratory Animal Care (APLAC).

Note that full information on the approval of the study protocol must also be provided in the manuscript.